Autoreferat: ENGLISH VERSION

1. Imię i nazwisko: Carmine Autieri

2. Stopnie naukowe:

25 May 2012. Ph.D. graduated at the Università degli Studi di Salerno (Italy) with maximum grade. Ph.D. thesis entitled **Interplay of spin-orbital correlations and structural distortions in Ru- and Cr- based perovskite systems** in the group of Prof. C. Noce and Dr. M. Cuoco. 9 months stay at the Jülich Forschungszentrum (Germany) as a guest student in the group of Prof. E. Pavarini.
28 October 2008. Master in solid state physics at the Università degli studi di Salerno (Italy). Graduated with top marks and honours, master thesis entitled **Extended impurity in Sr_2RuO_4**.
14 September 2006. Bachelor in physics at the Università degli studi di Salerno (Italy). Graduated with top marks and honours, diploma thesis entitled **Bloch theorem: formulation and applications**.

3. Zatrudnienie:

1 June 2018-Now. Doctor with advanced research and development experience at the "International Centre for Interfacing Magnetism and Superconductivity with Topological Matter" (MagTop) as expert in *ab-initio*. The position is equivalent to Assistant Professor. Magtop is a division of the Instytut Fizyki Polskiej Akademii Nauk (IFPAN). The website of the MagTop division is http://www.magtop.ifpan.edu.pl
1 May 2016-14 February 2018. Postdoc position at the SPIN-CNR in the UOS L'Aquila/Chieti (Italy) working at the project Magister (Magnetic Information Storage in Antiferromagnet Spintronic Devices) in the group of Dr. S. Picozzi. More information at http://nabis.fisi.polimi.it/projects/magister/.
1 May 2013-30 April 2016. Postdoc position at the Uppsala University (Sweden) in the group of Prof. B. Sanyal and Prof. O. Eriksson.
1 May-4 July 2014/1 July-30 November 2015. Guest at the Seagate Company in Derry (UK) working on simulations about the perpendicular magnetic record and the heat assisted magnetic record technology.
25 May 2012-30 April 2013. Postdoc position at the Jülich Forschungszentrum (Germany) in the group of Prof. E. Pavarini.

4. Omówienie osiągnięcia naukowego będącego cyklem siedmiu artykułów:

p1. **C. Autieri**, M. Cuoco and C. Noce: Structural and electronic properties of Sr_2RuO_4-$Sr_3Ru_2O_7$ heterostructures. Phys. Rev. B **89**, 075102 (2014). Preprint available at https://arxiv.org/abs/1211.4739 (IF=3.736).
p2. **C. Autieri** and B. Sanyal: Unusual ferromagnetic $YMnO_3$ phase in $YMnO_3$-$La_xSr_{1-x}MnO_3$ heterostructures. New J. Phys. **16**, 113031 (2014). (IF=3.558).
p3. S. Roy, **C. Autieri**, B. Sanyal and T. Banerjee: Interface control of electronic transport across the magnetic phase transition in $SrRuO_3$/$SrTiO_3$ heterointerface. Sci. Rep. **5**, Article number: 15747 (2015). Preprint available at https://arxiv.org/abs/1511.01933 (IF=5.228).
p4. **C. Autieri**: Antiferromagnetic and xy ferro-orbital order in insulating $SrRuO_3$ thin films with SrO termination. J. Phys. Condens. Matter. **28(42)**:426004 (2016). (IF=2.649).
p5. D. J. Groenendijk, **C. Autieri**, J. Girovsky, M. Carmen Martinez-Velarte, N. Manca, G. Mattoni, A. M. R. V. L. Monteiro, N. Gauquelin, J. Verbeeck, A. F. Otte, M. Gabay, S. Picozzi, and A. D. Caviglia: Spin-orbit semimetal $SrIrO_3$ in the two-dimensional limit. Phys. Rev. Lett. **119**, 256403 (2017). Preprint available at https://arxiv.org/abs/1706.08901. (IF=8.839).
p6. M. Asa, G. Vinai, J. L. Hart, **C. Autieri**, C. Rinaldi, P. Torelli, G. Panaccione, M. L. Taheri, S. Picozzi and M. Cantoni: Interdiffusion-driven synthesis of cubic Chromium (III) oxide on $BaTiO_3$. Phys. Rev. Materials **2**, 033401 (2018). (IF=2.926).
p7. M. Asa, **C. Autieri**, C. Barone C. Mauro, S. Picozzi, S. Pagano and M. Cantoni. Disclosing antiferromagnetism in tetragonal Cr_2O_3 by electrical measurements. Phys. Rev. B **100**, 174423 (2019). Preprint available at https://arxiv.org/abs/1911.02596 (IF=3.736).

New phases of the transition-metal oxides

Content

I. INTRODUCTION

There is a consolidated evidence that the surfaces and the interface between different electronic states and quantum orders is a source of novel physical phenomena[1]. The interest for this research area points both to the underlying fundamental physics as well as to the high impact in applications based on heterostructures with new emergent functionalities with respect to their constituents.

We can have new structural, electronic, magnetic, ferroelectric, superconductive and topological phases in one of the two sides of the interface or properties that lives at the interface like the Schottky barrier or the 2D electron gas[2]. Moreover, we can have a coupling between different degrees of freedom in the two different sides of the interface[3] like the magnetoelectric effect or the exchange bias[4]. We can have different proximity effects where one material can induce a quantum order in the other side of the interface. The breaking of the inversion symmetry could lead to effect forbidden in the bulk like the Rashba effect. Finally, one of the important feature is the interface termination in case of surfaces or multilayer materials. For this reason, attention should be paid to the interface chemistry, which can favor the interdiffusion of atomic species and, under certain conditions, lead to the formation of radically different compounds with respect to the original constituents. The spin, orbital, charge and lattice degrees of freedom affected at the interface may lead to artificial materials with novel properties, opening too the possibility to make new devices.[5] We present an overview on the quantum phenomena occurring in the low connectivity limit in transition metal oxides (TMO) using the density functional theory (DFT).

TMO with perovskite structure are prototype systems to be exploited in this framework due to the large variety of correlated driven physical phenomena they exhibit, ranging from Mott insulator to unconventional superconductivity through all sorts of different spin-charge-orbital broken symmetry states[6]. Moreover, the recent achievements in the fabrication of atomically controlled TMO-based interfaces explain why they represent a unique opportunity to explore how spin, charge and orbital reconstruction at the interface may determine novel quantum states of matter [7–13]. From a general point of view, the reduced dimensionality and the low-connectivity limit at the interface and surface is certainly a driving force for setting novel quantum phases as it may enhance the electronic correlations against the kinetic energy. On the other hand, the degree of matching of the TMO forming the heterostructure, the character of the transition elements and how they get into contact at the interface are the source of complexity and of a wide variety of physical properties.

In this context, the Ruddlesden-Popper (RP) family $A_{n+1}B_nO_{3n+1}$ of Sr-based ruthenates, with n being the number of BO_2 layers in the unit cell, offers a distinct perspective for designing interfaces of TMOs made of homologue chemical elements. In the case of Sr-ruthenates (A=Sr, B=Ru), they exhibit different character of the broken symmetry states and their properties range from unconventional p-type superconductivity,[14] to metamagnetism,[15] or proximity to a quantum critical point,[16,17] along with the notable magnetic effects[18–21] as a function of n. In the case of Sr-based iridates (A=Sr, B=Ir), the compounds present lower Coulombian repulsion but much stronger spin-orbit coupling. We studied the metal-insulator transition in the ultrathin films of the last members of the RP series $SrMO_3$ (M=Ru,Ir) searching for the similarities and the differences between the two cases(**p4-p5**).

After we move to the interface between two different perovskites. We carry out calculations for the $Sr_2RuO_4/Sr_3Ru_2O_7$ superlattices. We show that such systems develop a significant structural rearrangement within the superlattice, which leads to a modification of the electronic structure close to the Fermi level. Compared with the pure Sr_2RuO_4 and $Sr_3Ru_2O_7$ phases, we find that the positions of the peaks in the density of states close to the Fermi levels get shifted. Then, by means of the maximally localized Wannier functions approach, we determine the effective tight-binding parameters for Ru bands and used them to discuss the modification of the electronic structure and the

collective behavior of superlattice with respect to the bulk phases(**p1**). Following the same strategy, we investigate also the interface between two elements $SrRuO_3$ and $SrTiO_3$ of different RP series. We describe our theoretical proposal for the anomalous properties of the kinematic transmission factor across the ferromagnetic transition (**p3**).

While at the interface between two Sr-based TMO, there was only one possible termination due to the presence of the SrO layers in both sides of the interface, in the LSMO/YMO heterostructre we also need to investigate the many possible interface terminations. While from experimental point of view, usually, it is possible to stabilize just one termination, different terminations can produce different properties. We will investigate mainly the interplay between different magnetic properties of the two sides of the LSMO/YMO interfaces(**p2**).

As a last example of new phases at the interface, we will discuss a new structural phase of the Cr_2O_3 at the interface between the perovskite $BaTiO_3$ and chromium. The Cr_2O_3 is one of the principal oxides of chromium and is used as a green pigment. The most stable phase of the Cr_2O_3 is the corundum phase. This tetragonal phase of chromium (III) oxide, although unstable in the bulk, can be synthesized in epitaxial heterostructures. Despite the structural difference with respect to the ordinary corundum α-Cr_2O_3 phase, we demonstrate both experimentally and theoretically that the electronic properties of the two phases are, to a large extent, equivalent. Theoretical investigation by density functional theory predicts an antiferromagnetic ground state for this compound with a lower critical temperature based on the reduced connectivity respect to the corundum phase. It was demonstrate experimentally antiferromagnetism up to 40 K in ultrathin films of tetragonal Cr_2O_3 (**p6-p7**).

The thesis is organized as follows. In the Sec. II we provide the general framework of the computational analysis. Sec. III is devoted to the presentation of the results concerning the metal-insulator transitions described in the reference **p4-p5**. In the Sec. IV we discuss the outcomes of our calculations about the structural properties of Sr-ruthenates oxide superlattices studied in the references **p1-p3**, while in the Sec. V we propose a possible explanation for a pure vertical shift described in reference **p2**. From the references **p6-p7**, we describe the new structural phase at the oxide interface in Sec VI. Finally, Sec. VII summarizes our results.

II. METHODS

We have performed DFT calculations by using the VASP package[22] if not specified differently. The core and the valence electrons were treated within the Projector Augmented Wave (PAW) method[23,24] with a cutoff of 400 eV or higher for the plane wave basis due to the presence of the oxygen atoms. We fixed the lattice parameters to the experimental values and performed the relaxation of the internal degrees of freedom by minimizing the total-energy difference to be less than $10^{-5}/10^{-6}$ eV and the remaining forces to be less than 5-20 meV/Å depending on the size and other properties of the system. In case of the surfaces, we have used 20 Å of vacuum. We adopted the PBE or PBEsol for the exchange-correlation functional[25,26] to determine the unknown internal coordinates at the interfaces and surfaces. The PBEsol is a generalized gradient approximation (GGA)[25] optimized for the structural relaxation in the bulk compounds and it was shown to give excellent results for Sr-based TMO. The Hubbard U effects on the transition metal sites were included within the GGA + U[27] approach using the rotational invariant scheme[28]. The Coulomb repulsion and the Hund coupling can be written as:

$$U_{m,m'} = \sum_{k=0}^{2l} b_k(m,m')F^k$$

$$J_{m,m'} = \sum_{k=0}^{2l} c_k(m,m')F^k$$

where l and m are the azimuthal and magnetic quantun number, the F^k are the Slater integrals while $b_k(m,m')$ and $c_k(m,m')$ are numerical matrix.[29] The Coulomb repulsion is U=F^0 while J_H=0.116F^2 for the d-orbitals. The Lichtenstein approach is rotationally invariant and considers all the terms of the sum, while other simplified approaches consider just the k=0 term. We always use the Lichtenstein approach since it better describes the multiplet splitting and it is almost equivalent from computational point of view to simpler approaches. We use a value of the Hund coupling constant $J_H = 0.15U$ that is in agreement with the results obtained using the constrained random phase approximation[30].

In the case of magnetic metals, the GGA+U strongly overstimates the magnetic moment respect to the experimental results, therefore we have used LDA for the magnetic Sr-ruthenates oxides. The Coulomb repulsion in DFT pushes away the electronic states from the Fermi level. In the insulating phases, this opens the gap solving the band-gap problem, while in the case of metals, the Coulomb repulsion increases the bandwidth. The increase of the bandwidth is unphysical, indeed, more accurate approach like LDA+DMFT produces a reduction of the bandwidth once applied

the Coulomb repulsion. Therefore, the Coulomb repulsion in DFT should be used carefully and should not be too large for the metallic phases.

Let us consider some details about the determination of the effective tight-binding Hamiltonian in an atomic-like Wannier basis. There are different ways to get the Wannier functions for the relevant electronic degrees of freedom including the orthogonalized projections of specific atomic orbitals on the Bloch wave-functions in a distinct energy window and downfolded muffin tin orbitals as well as Maximally Localized Wannier Functions (MLWF). Hereafter, to extract the character of the electronic bands at the Fermi level, we use the Slater-Koster[31] interpolation scheme based on the MLWF method.[32,33] Such approach is applied to the determination of the real space Hamiltonian matrix elements in the MLWF basis. After obtaining the DFT Bloch bands, the MLWFs are constructed using the WANNIER90 code.[34] Starting from an initial projection of atomic d-basis functions belonging to the t_{2g} or e_g sector and centered at the different transition metal sites within the unit cell on the Bloch bands, we get a set of d-like MLWF for each site within the different unit cells of the analyzed systems.

We shortly introduce the main concepts about the MLWFs procedure. We start by noticing that in general the Bloch waves can be expressed as a Bloch sum of atomic-like basis functions or Wannier functions. Indeed, assuming to have a group of N Bloch states $|\psi_{n\mathbf{k}}\rangle$ that is isolated in energy from the other bands in the Brillouin zone (BZ), one can construct a set of N localized Wannier functions $|w_{n\mathbf{R}}\rangle$ associated with a lattice vector $\mathbf{R}$ by means of the generalization of the following transformation:

$$|w_{n\mathbf{R}}\rangle = \frac{V}{(2\pi)^3}\int_{BZ}\left(\sum_{m=1}^{N} U_{mn}^{(\mathbf{k})}|\psi_{n\mathbf{k}}\rangle\right)e^{-i\,\mathbf{k}\cdot\mathbf{R}}d\mathbf{k}$$

where, $U^{(\mathbf{k})}$ is a unitary matrix that mixes the Bloch functions at a given $\mathbf{k}$-vector in the Brillouin zone, V is the volume of the unit cell while m and n are the band indexes. The choice of $U^{(\mathbf{k})}$ determines the structure of the Wannier orbitals. In Ref. 32 the authors demonstrated that a unique set of Wannier functions can be obtained by minimizing the total quadratic spread of the Wannier orbitals expressed in terms of the position operator $\mathbf{r}$ through the following relation $\Omega = \sum_{n=1}^{N}\left[\langle\mathbf{r}^2\rangle_n - \langle\mathbf{r}\rangle_n{}^2\right]$ with $\langle O\rangle_n = \langle w_{n0}|O|w_{n0}\rangle$. For the case of entangled bands, one has to introduce another unitary matrix that takes into account the extra Bloch bands in the energy window upon examination. Such matrix is also obtained by minimizing the functional Ω.[33] Once a set of MLWFs is determined the corresponding matrix Hamiltonian is given by a unitary transformation from the diagonal one in the Bloch basis.

To extract the low energy properties of the electronic bands, we have used the Slater-Koster interpolation scheme as implemented in Wannier90.[34] In particular, we have fitted the electronic bands, in order to get the hopping parameters and the spin-orbit constants. This approach has been applied to determine the real space Hamiltonian matrix elements in the maximally localized Wannier function basis, and to find out the Fermi surface with a 50×50×50 k-point grid.

The resulting real space representation of the Hamiltonian in the MLWF basis can be expressed as

$$\tilde{H} = \sum_{\mathbf{R},\mathbf{d}}\sum_{n,m} t_{nm}^{\mathbf{d}}\left(\tilde{c}_{n,\mathbf{R}+\mathbf{d}}^{\dagger}\tilde{c}_{m,\mathbf{R}} + h.c.\right)$$

here $\tilde{c}_{n,\mathbf{R}}$ destroy an electron in the n orbital Wannier state $|w_{n\mathbf{R}}\rangle$. Then, the real space elements $t_{nm}^{\mathbf{d}}$ can be considered effective hopping amplitudes as in a tight-binding approach between MLWF separated by a distance $\mathbf{d}$ associated with the lattice vectors.

The Wannier method is really powerful for the TMO since the oxygen p-states are completely occupied and they do not overlap or weakly overlap with the d-orbitals of the transition metal. This allows to extract the model hamiltonian for the t_{2g} or e_g subsector. In other class of materials like the picnitides, the minimal model could be much difficult to extract using the Wannier method.[35,36]

III. METAL-INSULATOR TRANSITION IN $SrMO_3$ (M=Ru, Ir) ULTRATHIN FILM

Through interface and strain engineering it is possible to tailor the delicate balance between competing energy scales and control the ground state of complex oxides[37,38]. In the two-dimensional (2D) limit, the coordination of constituent ions at the interfaces is reduced, typically yielding a decrease of the electronic bandwidth W. At a critical thickness depending on the relative magnitude of W and the Coulomb repulsion U, a metal-insulator transition can occur[39]. This approach has been applied to study the dimensionality-driven metal-insulator transition (MIT) in 3d transition metal oxides such as $SrVO_3$ and $LaNiO_3$, where a transition from a bulk-like correlated metallic phase to a Mott or static ordered insulating phase occurs in the 2D limit[37,40–42]. Recent study found a similar MIT also in ultrathin films of ruthenates with mixed cation[43] and in Sr-ruthenates superlattice[44].

We consider the 4d and 5d oxide $SrMO_3$ (M=Ru,Ir) which are the last members of the RP series. In the three-dimensional limit, the SRO is an itinerant ferromagnet while the SIO is a narrow-band semimetal bordering a Mott transition due to a combination of strong spin-orbit coupling (SOC) and electron correlations. We investigate the thickness-dependent electronic properties of ultrathin $SrMO_3$ and discover a transition from a semimetallic to a correlated insulating state below 4 unit cells for both compounds. Our DFT calculations reproduce the critical thickness of the transition and show that the opening of a gap in ultrathin films requires antiferromagnetic order. While both metal-insulation transition are bandwidth driven, the main differences between the two cases is the role of the spin-orbit coupling and Coulombian repulsion.

A. The Ru case: the role of the electronic correlations-p4

When thin films of $SrRuO_3$ are epitaxially grown on $SrTiO_3$, films less than 2 unit cells thick were found to be insulating[45–47]. This metal-insulator transition is not observed in any other Sr-ruthenates compound, but an insulating behaviour was already observed in the isoelectronic Ca-ruthenates series. Indeed, the $Ca_{n+1}Ru_nO_{3n+1}$ tend to behave as antiferromagnetic (AFM) insulators, where the Ca atoms just modify the structural distortions bringing the system in a Mott insulator. The Ca_2RuO_4 compound is a Mott insulator which exhibits G-type AFM ordering and a metal-nonmetal transition occurring simultaneously with a first-order structural phase change[48–50].

We investigate the competition between the metal ferromagnetic phase and the antiferromagnetic phase in $SrRuO_3$ thin films. The reduced kinetic energy and the surface reconstruction might drive the system to a Hubbard AFM insulator. We also investigate the orbital order properties at the surface and we compare with other orbital ordering found in ruthenates[51,52].

The $SrRuO_3$ surface was already analysed by Mahadevan *et al.*[53] catching the insulating phase. We study the experimental surface with SrO termination[54,55] of Sr-ruthenates systems and using the best exchange correlation functional for the $SrRuO_3$ compound[56] and we propose some analogies with Ca-ruthenates. We investigate deeply the structural, magnetic and electronic properties up to 4 unit cells comparing the results with respect to other quasitwodimensional ruthenates. An other study analyzed the quantum confining of the electrons in the $SrRuO_3$ layers[47]. This explains the weakness of the ferromagnetic (FM) solution, but cannot explain the insulating AFM state.[57].

Structural optimization was performed in LSDA+U approximation separately for the ferromagnetic and antiferromagnetic case. We simulate the FM and the G-type AFM phase and calculate the energy difference ΔE

$$\Delta E = E_{AFM} - E_{FM} \tag{1}$$

between these two magnetic phases per Ru atom. In this Section we present the structural and electronic properties of the bulk system and surface. Before considering the surface, we analyze the electronic structure of the bulk $SrRuO_3$ phase. We show that we are able to reproduce the bulk electronic properties within the computational scheme above mentioned. After we increase the Coulomb repulsion as expected for the surface and we study the surface reconstruction of 1 unit cell in both magnetic phases. Moreover we compare the 1 unit cell antiferromagnetic phase with the bulk Ca_2RuO_4. We examined the $SrRuO_3$ films as function of the thickness in order to analyze the nature of experimentally observed metal-insulator transition as function of the number of layers.

1. Slab with 1 unit cell of $SrRuO_3$

We simulate a slab with three layers of $SrTiO_3$ and one layer of $SrRuO_3$. If we do not perform surface reconstruction, the AFM solution converges to a metallic phase that is not the ground state. Performing the full relaxation of the atomic positions, we find a strong reconstruction with a shrink of the surface layer due to under-coordinated surface atoms, this was also found in other perovskite oxide surfaces[58]. Moreover, we find that the oxygen atom of the SrO termination goes outer as was found in the surface $SrTiO_3$[59]. These effects produce buckling in the SrO layer as shown in Fig. 1-(a), this is expected considering that the buckling of the SrO layer is very sensitive to the surface or interface[60]. The distance of oxygen plane from the strontium plane at the surface is 0.206 Å for the AFM surface and 0.216 Å for the FM surface. This geometrical structure of the SrO surface layer is the very close to the quasitwodimensional system Sr-ruthenates and their heterostructures[60]. Because the Sr-O bond changes at the surface, we can expect also modification in the covalency of the oxygen. The covalency plays a crucial role as was shown in the similar compound $CaRuO_3$[61,62] and influences the value of magnetization.

Now, we investigate the DOS near the Fermi level projecting on the d_{xy} and $d_{\gamma z}$=d_{xz}+d_{yz} in Fig. 2. The twodimensionality of this surface with 1 u.c. produces a smaller bandwidth respect to the bulk phases. For the

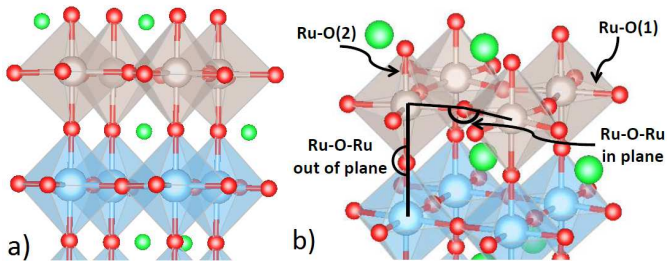

FIG. 1: Buckling of the SrO surface (left panel) and definitions of the Ru-O bonds and Ru-O-Ru bond angles (right panel). We use the same color notation for the atoms used in Fig. 6.

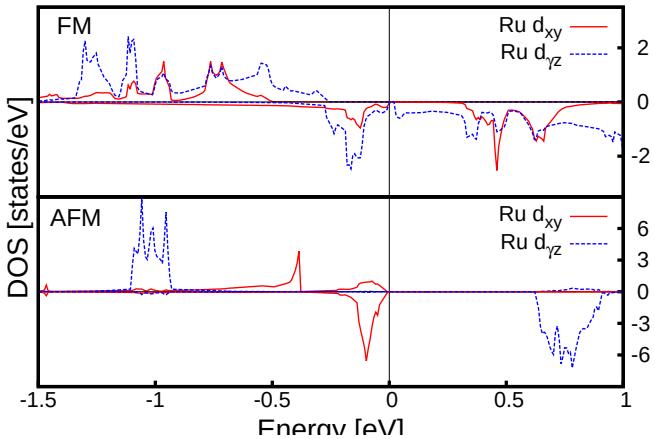

FIG. 2: d_{xy} (solid red) and $d_{\gamma z}$ (dashed blue) layer projected DOS for the FM and AFM $SrRuO_3$ with 1 u.c. at U=2.7 eV. At the surface, the occupied orbital is d_{xy} in the minority spin channel of the AFM phase. Majority (minority) spin is represented in the upper (lower) half of the panel. The DOS of the AFM phase is similar to the DOS of Ca_2RuO_4 at low temperature[51].

ferromagnetic phase we found the halfmetallic behaviour with a magnetization of 2 μ_B typical of LSDA+U for $SrRuO_3$[63] at U=2.0 eV, but it becomes insulating at 3.4 eV. Instead, the AFM phase is always insulating and it is the ground state for every value of U. At U=2.7 eV the gap in the FM phase is very small around 0.02 eV, while it is 0.6 eV in the AFM phase. In both cases, the low energy region is dominated by the t_{2g} electrons. The electrons are strongly confined to their layer in this system[47,64] and the influences of the Ti electrons on the $SrRuO_3$ is negligible. In the FM phase the entire t_{2g} sector is occupied in the majority spin channel and just one electron is present in the down spin channel. In the AFM phase we find a smaller bandwidth with respect to the FM case and the smaller bandwidth increases the band gap. The d_{xy} band on the surface is very tight, so the d_{xy} electrons are more localized than other electrons. Surprisingly, we find an inversion of the crystal field with respect to the bulk $SrRuO_3$[57]. Basically, the d_{xy} does not give contribution to the magnetization while the two $d_{\gamma z}$ bands are occupied in the up channel and are unoccupied in the down channel. This is also called xy ferro-orbital order and was already observed in Ca_2RuO_4 (Fig. 2 of reference 51). The structural reconstruction and the consequent inversion of crystal field are fundamental to stabilize the AFM phase. Indeed the superlattice $(SrRuO_3)_1/(SrTiO_3)_5$ is ferromagnetic[64] because there is no strong structural rearrangement, but for large strain the superlattice $(SrRuO_3)_1/(SrTiO_3)_1$ is found to be antiferromagnetic G-type[65]. In this case the effect of the tensile strain is replaced by the shrink of the c-axis, because the tensile strain in superlattice and the shrink at the surface have the same consequence on a fundamental ratio c/a.

2. *Comparison between the single layer $SrRuO_3$ and the bulk Ca_2RuO_4*

The strong similitude between the DOS of the single layer $SrRuO_3$ and the bulk Ca_2RuO_4 suggests to investigate and compare also other properties of the two systems. In Table I we report the geometrical properties defined in the Fig. 1-(b) and the magnetization of the $SrRuO_3$ and Ca_2RuO_4 bulk compared with the single layer $SrRuO_3$. Due to the symmetry broken the surface presents more values of the Ru-O bonds. First, we can observe the compression of

the octahedra in the single layer that favors the xy ferro-orbital order. In both Ca_2RuO_4 and single layer of $SrRuO_3$ the shortest bond is the Ru-O(2) bond, the bond along the c-axis. Both the bulk Ca_2RuO_4 and the single layer of $SrRuO_3$ show the Ru-O(1) bonds equal to 2.00 Å and the Ru-O(2) equal to 1.97 Å, while the Ru-O bonds in the bulk $SrRuO_3$ are all equal to 1.98 Å. The bond between the Ru and the oxygen atom of the surface is 1.95 Å due to the surface reconstruction. We define the rotation angle as half of the complementary angle of the Ru-O-Ru in plane bond angle and similarly we define the tilt angle as half of the complementary of the Ru-O-Ru out of plane bond angle. The rotation angle of the single layer $SrRuO_3$ is 12.6° and closer to the Ca_2RuO_4 respect to the bulk $SrRuO_3$. Instead, the small value of the tilt angle 1.2° can be attribute to the presence of $SrTiO_3$ that in the bulk has zero tilt angle. Also in other ruthenates surfaces it was reported a strong surface reconstruction that gives us a large rotation angle of 12° and a small tilt of 2.5°[68]. Due to the many similarities with Ca_2RuO_4 it will be interesting to investigate if also the metal-insulator transition as function of the temperature happens in the single layer $SrRuO_3$ above room temperature.

TABLE I: We report the geometrical properties of the octahedra for the single layer in LSDA+U compared with the experimental results of $SrRuO_3$[66] and Ca_2RuO_4[67]. The surface reconstruction has significant impact on the monolayer slab. The unit of the bond angles is degree, the unit of the bond length is angstrom and the magnetization is in Bohr magneton.

	$SrRuO_3$	Single layer	Ca_2RuO_4
long Ru-O(1)	1.9876	2.0013; 2.0007	2.0182
short Ru-O(1)	1.9809	2.0006; 1.9999	2.0042
Ru-O(2)	1.9835	1.9765; 1.9451	1.9731
Rotation	8.6	12.6	11.9
Tilt	8.6	1.2	11.2
Magnetization	1.6	2.0	2.0

TABLE II: We report the geometrical properties of the system calculated in LSDA+U for the experimental volume, the theoretical volume, the 1 u.c. surface and the 3 u.c. surface. The first value in the last column is for the surface layer, the middle is for the inner layer and the last is for the inner layer interfaced with $SrTiO_3$.

	Exp.	Th.	1uc	3uc
$\frac{l-s}{l+s}$ FM	0.0004	0.0004	0.0006	0.0009 / 0.0006 / 0.0005
$\frac{l-s}{l+s}$ AFM	0.0119	0.0097	0.0002	0.0011 / 0.0075 / 0.0092
Rotation FM	10.2	10.5	9.5	9.8 / 10.5 / 9.7
Tilt FM	9.9	10.0	4.5	8.7 / 9.3 / 6.2
Rotation AFM	9.7	9.9	12.6	12.6 / 10.2 / 9.6
Tilt AFM	12.7	12.7	1.2	8.4 / 11.7 / 6.9

3. Multilayer Slabs

Also in the case of multilayers of $SrRuO_3$, we find a structural rearrangement at the surface with the shrinking along the c-axis and the oxygen outer. We analyze in details the case of three $SrRuO_3$ layers. The $SrRuO_3$ regions is composed by the surface layer, an inner layer and the inner layer interfaced with the $SrTiO_3$. We report in Table II the comparison of the geometrical properties among the experimental volume, the theoretical volume, the surface with 1 u.c. and the surface with 3 u.c.. The Jahn-Teller distortion creates a long (l) and a short (s) Ru-O bond in the ab plane. We calculate the quantity $\frac{l-s}{l+s}$, that is an indication of the strength of the Jahn-Teller effect. We can observe that in all the case the tilt angle closer to the interface is always smaller than 7° because the $SrTiO_3$ compound prefers to have the tilt angle equal to zero. In the FM phase the Jahn-Teller increases at the surface, while the rotation and tilt angles decrease at the surface. The situation is more interesting for the AFM phase. The Jahn-Teller at the surfaces is close to the FM phase, but in the bulk and inner layers the Jahn-Teller increases by one order of magnitude. This is due to a structural change in the AFM bulk. We always have two equal bonds and a very short bond, but the shortest Ru-O bond is not along the c-axis as in the single layer but it is in the ab plane. This effect also creates the inversion of the tilt and rotation angle with the tilt angle that becomes larger than the rotation

angle in bulk and inner layers. In the bulk the system is not able to reproduce the compression of the octahedra along the *c*-axis. This kills the xy ferro-orbital order and inhibits the antiferromagnetic phase in the bulk. The rotation angles at the surface are larger than 12° closer to the Ca_2RuO_4.

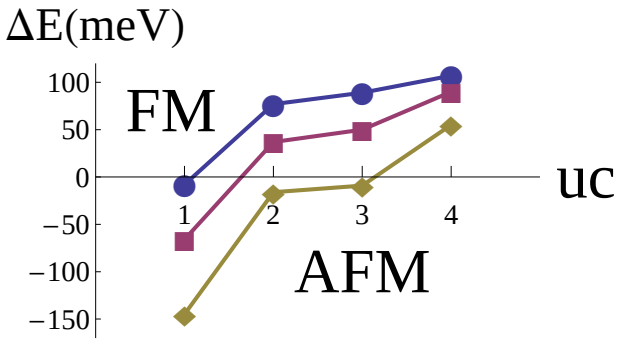

FIG. 3: Energy differences between ferromagnetic and antiferromagnetic phase as function of the number of unit cell per formula unit for U= 2.0 (circle), 2.7 (square) and 3.4 eV (triangle). Lines are guides to the eyes. We can see that the first layer gives a strong contribution to the AFM phase.

We study the stability of the magnetic phase in Fig. 3 as function of the Coulomb repulsion and number of layers. The number of layers is related to the bandwidth. A larger number of layers produces a larger bandwidth in this system. The AFM phase is very stable for one u.c. being the ground state for every value of U. We can see that the surface layer gives a strong contribution to the stabilization of the AFM phase with $\Delta E \approx$ -150 meV for U=3.4 eV. At 2 u.c. ΔE jumps to an higher value and this jump can be attributed to the lost of the orbital order. With 1 u.c. we have the xy ferro-orbital order. When we add more $SrRuO_3$ layers, the orbital order disappears in the inner layers and the system tends to become ferromagnetic. At 2 and 3 u.c., the ground state depends on the value of U because the two phases are really close in energy. At 4 u.c., the ferromagnetic phase becomes definitively the ground state for every value of U used in this calculation. In the case of 4 u.c. we have 2 inner layers not interfaced with $SrTiO_3$, these inner layers strongly prefer to be ferromagnetically coupled therefore the system with 4 u.c. becomes ferromagnetic. The increasing of U enlarges the band gap and stabilizes the AFM insulating phase. The critical thickness depend on the Coulomb repulsion, for U=2.0 and 2.7 eV the system is insulating just for 1 u.c. while the system is insulating until 3 u.c. for U=3.4 eV.

The eventual first-order metal-insulator transition, analogue to the transition in Ca_2RuO_4, should have a critical temperature strongly dependent on the number of unit cells with the critical temperature that should be higher for the thinner samples. Moreover, a coexistence of ferromagnetic and antiferromagnetic phase was suggested[46] and this coexistence is compatible with the theorethical scenario described in this work[69]. This coexistence of the metallic and insulating phase, similar to the one predicted for the surface of the ruthenates oxides, was recetly found in Ca_2RuO_4.[70]

B. The Ir case: the role of the spin-orbit coupling-p5

$SrIrO_3$ is the only metallic member of the RP series of strontium iridates $Sr_nIr_nO_{3n+1}$. On the other end of the series, the quasi2D Sr_2IrO_4 (n=1) is a Mott insulator with canted antiferromagnetic order. Despite the extended 5d orbitals, narrow, half-filled J_{eff}=1/2 bands emerge due to the strong SOC ($\approx$ 0.4/0.5 eV) and even a relatively small U is sufficient to induce a spin-orbit Mott ground state[71,72]. In $SrIrO_3$, the effective electronic correlations are smaller due to the threedimensional corner-sharing octahedral network[73], but the strong SOC causes a significant reduction of the density of states (DOS) at the Fermi level. Together with octahedral rotations that reduce the crystal symmetry, this places the material at the border of a Mott transition and gives rise to an exotic semimetallic state[74,75]. To study changes in electronic structure between the two end members of the RP series, previous studies have focused on varying the number of $SrIrO_3$ layers in $[(SrIrO_3)_m; SrTiO_3]$ superlattices[76–80].

First-principles DFT calculations were performed using the PBEsol for the exchange-correlation functional with SOC. The Hubbard U effects on the Ir and Ti sites were included. To find a unique value of the Coulomb repulsion for the Ir 5d states, U was tuned in order to reproduce the experimental semimetallic behavior at 4 u.c. Using this approach we obtained U=1.50 eV, which is in good agreement with the typical values used for correlated Ir compounds[81].

As the film thickness is reduced, the resistance continuously increases and two different regimes can be identified. For t>=4 u.c., the films show metallic behavior (see **p5**). Thinner films (t $<$ 4 u.c.) display insulating behavior.

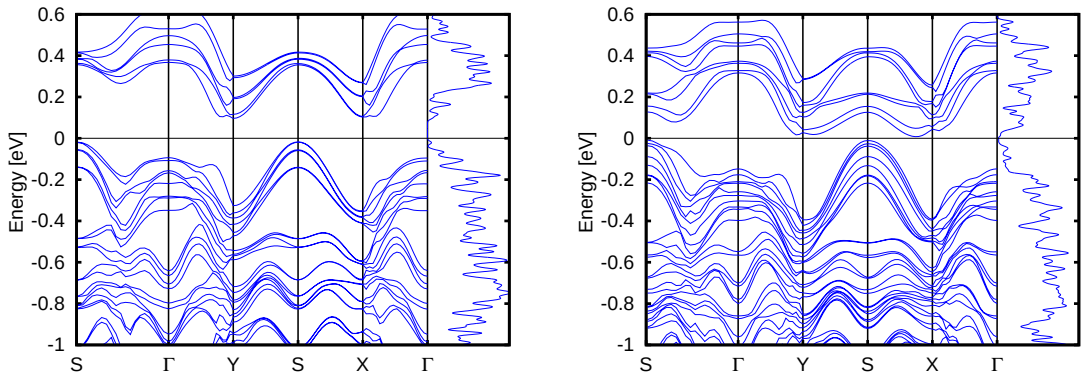

FIG. 4: Calculated electronic structure for 3 u.c. (left panel) and 4 u.c. (right panel) $SrIrO_3$ films on tetragonal $SrTiO_3$ with U=1.50 eV. Right: the corresponding DOS per formula unit as a function of energy.

Hence, it is apparent that $SrIrO_3$ films undergo a semimetal-insulator transition between 4 and 3 u.c. This is in good agreement with photoemission measurements, which show the disappearance of the Fermi cutoff below 4 u.c. and the opening of a charge gap[82]. Further insights into the anomalous behavior in the semimetallic state and the electronic structure near the MIT are obtained by measuring the local DOS across the Fermi energy E_F by STS measurements. Differential conductance spectra acquired at 4 K on films of 4, 6, and 10 u.c. thickness show V-shaped behavior with a linear dependence of the DOS for both occupied and unoccupied states. Therefore, the evolution of the DOS at E_F reflects the approach of the MIT, where the 4 u.c. film is on the verge of a gap opening.

To study the electronic and magnetic structure of $SrIrO_3$ in the 2D limit, we perform first-principles calculations. We first consider how the properties of bulk $SrIrO_3$ evolve as a function of U. At low U, the system shows a nonmagnetic metallic state topologically protected by time-reversal symmetry[83]. Upon increasing U, a canted G-type antiferromagnetic (AFM) metallic state with a net in-plane magnetic moment emerges[77]. A further increase of U opens a gap, leading to a G-type AFM insulating state[84] like in $[(SrIrO_3)_mSrTiO_3]$ superlattices[77]. Since both U and the breaking of time-reversal symmetry are required to open the gap, insulating $SrIrO_3$ is located in the intermediate region between a Slater- and a Mott-type insulator. The same qualitative results were obtained in other Ir compounds[85].

When moving from bulk $SrIrO_3$ to $SrIrO_3/SrTiO_3$ heterostructures, compressive strain, reduction of the bandwidth and an increase of U have to be taken into account. Compressive strain ($\simeq 1\%$) favors the metallicity[76] because of the increased bandwidth[81]. The other two effects favor the insulating state[86] and are needed to observe the semimetallic or insulating phase in $SrIrO_3$ ultrathin films. We note that U is typically larger in thin films than in superlattices since in the latter the $SrIrO_3$ layers are expected to exhibit a relaxation of octahedral tilts towards bulk values facilitated by tilts in the $SrTiO_3$ layers[87]. For our calculations we focused on the thickness range in the vicinity of the MIT and computed the band structure of 3 and 4 u.c. $SrIrO_3$ layers on a $SrTiO_3$ substrate in the slab geometry (including vacuum) for U=1.50 eV. The results are shown together with the corresponding DOS in Figs. 4(a) and 4(b), respectively. The bandwidth reduction when going from 4 to 3 u.c. results in a localization of the carriers, and triggers a transition from a semimetallic to an AFM insulating state. Even for a single layer of $SrIrO_3$ on $SrTiO_3$ the nonmagnetic case is found to be metallic, and AFM ordering is required for the opening of a gap[82]. The electronic structure of the 4 u.c. film shows a gap-closing behavior, consistent with STS. In the case of 3 u.c. the gap is 60 meV; its precise value is, however, crucially dependent on many effects such as octahedral distortions, magnetic order, strain, connectivity, and Coulomb repulsion. Near the Fermi level, the DOS is dominated by a 5d t_{2g} contribution as in bulk $SrIrO_3$. Hence, by reducing the thickness, we approach a state closer to $J_{eff}=1/2$ as in Sr_2IrO_4.

C. Summary for the metal-insulator transitions

In conclusion, we determined the structural, magnetic and electronic properties of $SrMO_3$ (M=Ru,Ir) thin films grown on $SrTiO_3$ substrate with different numbers of unit cell. We have shown that $SrMO_3$ (M=Ru,Ir) can be driven into a correlated insulating state in the 2D limit. While in both cases the metal-insulator transition is simply due to the electron localization and consequently to the reduction of the bandwidth with the appearance of the insulating *G*-type antiferromagnetic phase, the Coulombian repulsion, the SOC and structural properties play a different role in the two cases.

In the $SrRuO_3$, we have shown that surface formation generally leads to the shrinking of the *c*-axis due to the

under-coordinated oxygen atoms at the surface, the oxygen outer and a consequent inversion of the crystal field of the surface layer. The $SrRuO_3$ surface presents many similarities (rotation angles, projected DOS and d_{xy} ferro-orbital ordering) with the Ca_2RuO_4 compound. Instead, in the $SrIrO_3$ the MIT is supported by the SOC while the electronic correlations is lower than the $SrRuO_3$. The close proximity of $SrIrO_3$ to a correlated insulating state is further corroborated by STS measurements, showing a V-shaped DOS similar to the doped $J_{eff}=\frac{1}{2}$ Mott insulator Sr_2IrO_4.

IV. STRUCTURAL, ELECTRONIC AND MAGNETIC PROPERTIES AT THE Sr-RUTHENATES OXIDES INTERFACE

In the previous Section, we investigate the how the surface reduces the electron bandwidth and modify other properties of the TMO. In this Section, we show that also the structural reconstruction at the interface of the transition metal oxides can modify their physical properties due to the breaking of the crystal symmetry introducing atomic shifts perpendicular to the interface and inducing new octahedral rotations. In this Section, we will present the study of the modifications that appears at the $Sr_2RuO_4/Sr_3Ru_2O_7$(**p1**) and the $SrRuO_3/SrTiO_3$(**p3**) interface. Moreover, we present the consequences of these modifications on the collective modes and the kinetic transmission factor across the interface.

A. Shift of the VHS at the $Sr_2RuO_4/Sr_3Ru_2O_7$ interface-p1

Two experimental achievements have triggered a significant interest towards interfaces made by ruthenates RP-members. First, the presence of an eutectic point in the chemical phase diagram of the SrRuO perovskites allows one to get natural interfaces in the form of single crystalline micrometric domains between adjacent members of the series. In this respect, we mention that Sr_2RuO_4-$Sr_3Ru_2O_7$[88,89] and $Sr_3Ru_2O_7$-$Sr_4Ru_3O_{10}$[90] eutectics have been achieved. The investigation of the collective behaviour of the eutectic phases indicates a relevant role of the interface physics, and their superconducting and magnetic properties turn out to be quite different if compared to the homogeneous single crystalline ones.[91–93]

The other important reason to study interfaces made of Sr-based ruthenates is that thin films of the series from n=1 to n=5[94,95] have been successfully grown. While the magnetic states are usually obtained in the Sr-RP members in the shape of thin films, it is quite remarkable to underline the preparation[96] of superconducting thin films of Sr_2RuO_4 whose difficulty is due to the strong sensitivity of the spin-triplet pairing to disorder. Thus, the synthesis of superlattices based on different RP-members is in principle an achievable task, increasing the research in designing superlattices or heterostructures by fully employing the different character of the broken symmetry states realized within the Sr-RP family as a function of n.

Taking into account the above mentioned motivations, the aim of the subsection is to analyze the structural and electronic properties of Sr_2RuO_4-$Sr_3Ru_2O_7$ superlattices. The focus is on the superlattice structures $(Sr_2RuO_4)_3$-$(Sr_3Ru_2O_7)_3$ with 3 layers of both the number of n=1 and n=2 unit cells in the heterostructure. Hereafter we denote as HET33 the superlattice structure. Since the systems we investigate in the paper are paramagnetic, we perform spin-unpolarized first-principles density functional calculations[97] by using the plane wave ABINIT package.[98] Then, we first perform the calculation of the relaxed crystal structure and of the energy spectra for the Sr_2RuO_4 and $Sr_3Ru_2O_7$ bulk phases, and then we implement the same computational scheme for the superlattice. We would like to note that standard functionals based on local density approximation may tend to overestimate the volume producing inaccurate ratio between the c- and a-axes.[101] This problem is encountered for the analyzed class of ruthenate oxides, especially for the $Sr_3Ru_2O_7$ bulk phase. Thus, to get a more accurate determination of the volume and lattice constants in the study of the superlattice made of the first two RP members of the series, we employ the exchange-correlation of Wu and Cohen[99] optimized for the relaxation of bulk systems. The fully relaxed volume and the atomic positions have been determined for the bulk and the superlattice configuration. Therefore, we can discuss in detail the role played by the interface examining how the structural modifications of the Sr-O and Ru-O bonds affect the electronic distribution.

The maximally localized Wannier functions approach is then applied to extract the effective tight-binding parameters between the $4d$-t_{2g} Ru orbitals. The outcome is used to discuss the modification of the electronic structure of the superlattice, as well as its interrelation with the structural properties and the bulk phases. This allows one to extract the structural and the electronic features of the different RuO_2 layers depending on the character of the neighboring ones. This allow us to check the variation of the peak positions in the density of states close to the Fermi level. We find that these peaks get shifted compared to the bulk case, and the balance between the renormalization of the

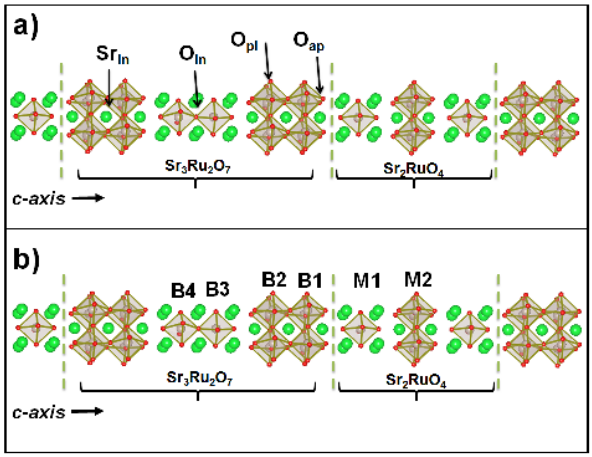

FIG. 5: (color online) Notation about the labelling of the atoms within the superlattice. O_{pl} is the planar oxygen, O_{ap} is the apical oxygen, O_{in} denotes the intra-bilayer oxygen, and Sr_{in} the intra-bilayer strontium. Sr_{in} and O_{in} are present only in the $Sr_3Ru_2O_7$ side of the heterostructure. The remaining strontium atoms are labelled Sr.

bandwidth of the d_{xy} band and the crystal field splitting results into a change of the Van Hove singularities (VHS) positions in the superlattice with respect to the pure phases.

1. *Structural properties of the bulk and Sr_2RuO_4-$Sr_3Ru_2O_7$ superlattice*

A complete structural analysis was performed in the paper **p1**. We will focus Δz displacement along the c-axis of the Ru atoms with respect to the planar oxygens, and the variation of the Ru-O-Ru bond angles. The results are summarized in Table III from which we can infer two different trends for Δz in Sr_2RuO_4 and $Sr_3Ru_2O_7$. Indeed, as far as Δz for Sr_2RuO_4 is considered, we see that in the inner region of the HET33 structures this quantity is zero, i.e. there is no variation of the displacement along the c-axis of Ru ions compared to the pure phase. On the other hand, at the interface a small Δz is produced and the Ru atom goes far from the interface. Concerning the $Sr_3Ru_2O_7$, a Δz is already present in the case of the bulk phase, but an enhancement of the amplitude of Δz is deduced at the interface.

Referring to the Ru-O-Ru bond angles, there is no significant variation in the inner layers of the Sr_2RuO_4 side of the superlattice for the HET33 configurations, while at the interface the displacement along the c-axis of the Ru atoms produces a reduction of the Ru-O-Ru bond angle. The situation is completely different for the $Sr_3Ru_2O_7$ side of the hybrid structure. Indeed, a deviation from the pure phase angle is found, as well as in the inner region, exhibiting a dependence whose amplitude is related to the size of considered superlattice. However, the bond angle increases with respect to the inner region in both cases. The rotation angle of the octahedra, that is half of the supplementary of the Ru-O-Ru bond angle, decreases at the interface in the $Sr_3Ru_2O_7$ phase.

The change of the atomic positions reveals a tendency of the ions positively charged in the ionic picture to move in the direction of the Sr_2RuO_4 side, while the negative ones go in the opposite direction towards the $Sr_3Ru_2O_7$ side. We note that two bonds are strongly modified at the interface: the distance between the ruthenium and the apical oxygen, and the distance between the Sr ion and the apical oxygen along the c-axis, the other in-plane modifications being smaller. At the interface between Sr_2RuO_4 and $Sr_3Ru_2O_7$, two different SrO insulator planes meet. The different geometrical configurations of SrO planes make near the Sr of the n=2 phase and the O_{ap} of the n=1 phase, so that a new bond not present in the bulk is created, and this new bond may drive the interface reconstruction.

2. *Sr_2RuO_4-$Sr_3Ru_2O_7$ superlattice: electronic properties*

We have determined the electronic properties of HET33 heterostructures with the aim to analyze the modifications of the spectra within the superlattice and in comparison with the bulk phases as well as to extract the interrelation between the structural changes and the electronic dispersions. Based on the detailed analysis of the structural properties we expect that the effective hopping and the hybridization parameters for the energy bands at the Fermi level are influenced both in the amplitude and in the character. Also a rearrangement of the on-site Ru $4d$ energies is

TABLE III: Ru-O-Ru bond angles and displacement of Ru in the several cases studied. At the interface, the modification of the Ru-O-Ru bond angle in Sr_2RuO_4 it is due to the Ru displacement along the *c*-axis, no rotations are found. The unit of the Δz is Å.

	Exp. [108,112]	Th. Bulk	Inner RuO_2 layers HET33	Interface HET33
Δz in Sr_2RuO_4	0	0	0	0.007
Δz in $Sr_3Ru_2O_7$	0.017	0.033	0.030	0.037
Ru-O-Ru bond angle in Sr_2RuO_4	180.0°	180.0°	180.0°	179.6°
Ru-O-Ru bond angle in $Sr_3Ru_2O_7$	163.9°	158.1°	157.4°	157.5°

expected to influence the $4d$ energy splitting due to the flattening and elongation of the RuO_6 octahedra within the superlattice.

We point out that the position and the intensity of the VHS depend essentially on two parameters: the energy on-site and the effective electronic parameters related to the Ru-Ru hopping amplitudes, and it is strictly related to the character of the momentum dispersion around the VHS point. In our case, we recall that this singularity is located within the d_{xy} band. To understand the origin of the shift between the VHS for the Sr_2RuO_4 we use the following approximated expression for the dispersion of the d_{xy} band:

$$\varepsilon_{xy}(\mathbf{k}) \approx \varepsilon^0_{xy} + t^{100}_{xy,xy}(cosk_x + cosk_y) + 4t^{110}_{xy,xy}cosk_x cosk_y,$$

where the chemical potential is set to zero. Considering that the Sr_2RuO_4 VHS is placed at the point (0,π) or (π,0) of the Brillouin zone, the energy of the VHS ε_{VHS} is given by:

$$\varepsilon(0,\pi) = \varepsilon_{VHS} \approx \varepsilon^0_{xy} + 4|t^{110}_{xy,xy}|,$$

where ε^0_{xy} depends on the crystal field and $|t^{110}_{xy,xy}|$ is inversely proportional to a power of the lattice constant a and directly proportional to a power of the the cosine of the rotation angle.[31] For instance, at the interface of the heterostructure in the Sr_2RuO_4 side there is a reduction of the hopping parameter with respect to the inner layer, but the variation of the crystal field tends to balance this effect reducing the difference of the ε_{VHS} between the interface and the inner layer. We may also estimate the shift of the VHS energies by comparing the bulk and the superlattice parameters. Hence, in the Sr_2RuO_4 case, the reduction of a in the heterostructure increases $|t^{110}_{xy,xy}|$, and subsequently ε_{VHS}. On the contrary, for the bilayer compound the superlattice VHS singularity is closer to Fermi level than in the bulk $Sr_3Ru_2O_7$. This is mainly due to the change of the d_{xy} bandwidth and of the crystal field splitting driven by the rotation and flattening or elongation of the octahedra.

Let us comment on the connection between these results and possible experimental consequences. A first potential link derives from the modification of the density of states close to the Fermi energy. The resulting DOS for the Ru xy band at the interface in the Sr_2RuO_4 side of the superlattice turns out to be greater than that in the uniform Sr_2RuO_4. Hence, the reduction of the bandwidth of the Ru xy band in the superlattice would point towards an enhancement of the correlations at the interface. These feature indicate a tendency toward the increase of the superconducting critical temperature either viewed in a Bardeen-Cooper-Schrieffer scenario or in a correlated driven pairing. Furthermore, the growth of the DOS at the Fermi level and the change in the effective bandwidth may also lead to a ferromagnetic instability within a Stoner picture supporting the possibility that the superlattice could exhibit a ferromagnetic transition. Nowadays the only reproducible eutectic system so far available, i.e. the Sr_2RuO_4-$Sr_3Ru_2O_7$ system,[88] may offer the opportunity to analyze and compare the effects of the interfacing between the first two RP-members. Electric transport and muon spin measurements in this eutectic compound confirm the occurrence of superconductivity at a critical temperature higher than that observed in the *pure* Sr_2RuO_4, with an onset of about 2.5 K whose origin could be ascribed to the Sr_2RuO_4-$Sr_3Ru_2O_7$ interface.[91] Our study would support such a scenario though an analysis of the pairing strength at the interface is required to further understand how the superconductivity is modified at the boundary.

Starting from the outcome of the density functional analysis and to understand more deeply the differences in the electronic properties within the superlattice and with respect to the bulk Sr_2RuO_4 and $Sr_3Ru_2O_7$, we have determined the effective tight-binding Hamiltonian in the MLWFs basis. The output of the relevant electronic parameters connecting the Ru t_{2g}-like Wannier states is given in the Table IV for the case of the HET33 heterostructure. This is the more general case as it contains inequivalent inner RuO_2 layers for both the Sr_2RuO_4 and $Sr_3Ru_2O_7$ subsystems. Starting from the $Sr_3Ru_2O_7$ side of the heterostructure we note that the electronic parameters are quite homogeneous within the superlattice confirming the small variations in the DOS at the interface and in the inner RuO_2 layers. In

TABLE IV: Effective hopping parameters along the direction $[lmn]$ and on-site energy in eV associated to the t_{2g}-like Wannier functions for the $(Sr_2RuO_4)_3$-$(Sr_3Ru_2O_7)_3$ superlattice. The connecting vector is expressed in terms of the integer set $[l\,m\,n]$ and the lattice constants a and c as $\mathbf{d} = l\,a\,\mathbf{x} + m\,a\,\mathbf{y} + n\,c\,\mathbf{z}$ for the related subsystems. The direction $00p$ connect the two ruthenium atoms within the bilayer of the $Sr_3Ru_2O_7$ side of the superlattice. B1 and B2 indicate the RuO_2 layers within the bilayer placed at the interface with the Sr_2RuO_4 and the $Sr_3Ru_2O_7$ side of the superlattice. B3 and B4 are the inner RuO_2 layers in the $Sr_3Ru_2O_7$ part. M1 and M2 indicate the interface and the inner RuO_2 layers within the Sr_2RuO_4 side. A schematic view of the structure and the labels is reported in Fig. 5b.

	$Sr_3Ru_2O_7$									Interface	Sr_2RuO_4				
orbital	B4-B3	B3		B3-B2	B2		B2-B1	B1		B1-M1	M1		M1-M2	M2	
$[l\,m\,n]$	[00p]	[000]	[100]	$[\frac{1}{2}\ \frac{1}{2}\ \frac{1}{2}]$	[000]	[100]	[00p]	[000]	[100]	$[\frac{1}{2}\ \frac{1}{2}\ \frac{1}{2}]$	[000]	[100]	$[\frac{1}{2}\ \frac{1}{2}\ \frac{1}{2}]$	[000]	[100]
xy-xy	-0.015	-0.423	-0.235	0.002/0.001	-0.423	-0.235	-0.016	-0.424	-0.237	0.002	-0.490	-0.380	0.002	-0.491	-0.381
yz-xy	0	0	±0.001	0.006/0.004/0.003	0	±0.001	0	0	±0.001	0.006/0.005	0	± 0.001	0.006	0	0
xz-xy	0	0	±0.016	0.006/0.004/0.003	0	±0.016	0	0	±0.020	0.006/0.005	0	0	0.006	0	0
yz-yz	-0.248	-0.335	-0.008	-0.023/-0.015/-0.011	-0.332	-0.008	-0.244	-0.315	-0.008	-0.021/-0.014	-0.307	-0.039	-0.020	-0.289	-0.039
yz-xz	0	0	±0.080	-0.025/-0.013/-0.003	0	±0.079	0	0	±0.077	-0.020/-0.009	0	0	-0.015	0	0
xz-xz	-0.248	-0.335	-0.285	-0.023/-0.015/-0.011	-0.332	-0.285	-0.244	-0.315	-0.277	-0.021/-0.014	-0.307	-0.280	-0.020	-0.289	-0.273

particular, the small modification of the local crystal field splitting, the bilayer splitting, and the t_{2g} bandwidth have a trend that follows the main structural changes. Indeed, since the octahedra are flattened for the outer RuO_2 layers at the interface (denoted as B1 and B2 in Fig. 5b) with respect to those in the inner layers (denoted as B3 and B4 in Fig. 5b) the energy associated to the $d_{\gamma z}$-like Wannier states is pushed up while the d_{xy} is not modified. Thus, the overall effect is to reduce the crystal field splitting, i.e. $\Delta_{cf} = |\varepsilon^0_{xy} - \varepsilon^0_{\gamma z}|$, at the interface with respect to the $Sr_3Ru_2O_7$ inner side of the superlattice. On the other hand, the bilayer splitting, the t_{2g} in-plane and out-of-plane nearest-neighbour hopping are basically uniform within the superlattice exhibiting a variation in a energy window of 2-10 meV. In such energy range the most significant modification is represented by the increase of the Ru-Ru γz nearest-neighbour hopping when moving from the interface to the inner layers. It is also worth noting that the hybridization amplitude between the xy and γz Wannier states is larger in the RuO_2 layers at the interface with the Sr_2RuO_4 than in the inner ones. At this point it is also relevant to analyze the differences of the effective tight-binding Hamiltonian between the superlattice $Sr_3Ru_2O_7$ side and the corresponding bulk phase. By the structural results we note that, due to a larger tilting of the octahedra with respect to the bulk, the in-plane xy Ru-Ru nearest-neighbour hopping is reduced in the superlattice. There occurs also a decrease of the γz Ru-Ru nearest-neighbour hopping but this is mainly driven by the flattening of the RuO_6 octahedra in the superlattice. The distortion of the octahedra influences also the crystal field and the bilayer splitting. The energy splitting Δ_{cf} is generally reduced in the superlattice if compared to the bulk phase except for the Ru atoms placed in the B1 outer layer of the interface bilayer (see Fig. 5b). The hybridization amplitude between the xy and γz Wannier states, which is a relevant parameter in setting the differences between the Sr_2RuO_4 and $Sr_3Ru_2O_7$ electronic structures, is doubled at the interface of the superlattice compared to that for the $Sr_3Ru_2O_7$ bulk phase.

Let us consider the electronic parameters for the Sr_2RuO_4 bulk and in the superlattice. Starting from the crystal field splitting we note that the elongation of the octahedra at the interface pushes down the energy of the Ru γz states. Such change, in turn, leads also to an increase of the Ru-Ru in-plane nearest-neighbour hopping moving from the inner layers to the interface ones. The remaining tight-binding parameters keep the symmetry connections as in the Sr_2RuO_4 bulk phase. Though the presence of a structural rearrangement at the Sr_2RuO_4-$Sr_3Ru_2O_7$ interface leads to flattening and rotation of the octahedra there are no extra induced hybridizations between the t_{2g}-like Wannier states. The comparison of the effective tight-binding Hamiltonian between the Sr_2RuO_4 side of the superlattice and the corresponding bulk phase shows that the in-plane xy Ru-Ru nearest-neighbour hopping is slightly reduced in the superlattice and the same happens to the γz orbitals. Hence, apart from a renormalization of the t_{2g} bandwidth and a modification of the crystal field splitting the electronic structure in the Sr_2RuO_4 keeps its qualitative features as far as it concerns, for instance, the nesting and the presence of the VHSs. We can also observe how the change of the xy nearest-neighbour hopping $t^{100}_{xy,xy}$ at the interface can be understood via the Ru-O-Ru bond angle. Indeed, the Ru-O-Ru angle at interface decreases for Sr_2RuO_4 and increases for Sr_2RuO_4 (Table III), consequently, the $t^{100}_{xy,xy}$ decreases for Sr_2RuO_4 and increases for Sr_2RuO_4 with respect to the inner layers values. Finally, we note that the broken mirror symmetry at the Sr_2RuO_4 interface induces an hybridization between the d_{xy} and d_{yz} orbitals in the [100] direction, as it can be inferred from an inspection of Table IV. We mention that this modification of the electronic structure in the presence of the atomic spin-orbit coupling has been proved to play an important role in the spin-triplet pairing state near the surface/interface of Sr_2RuO_4.[115]

B. Interface control across the magnetic phase transition in $SrTiO_3/SrRuO_3$ film-p3

We employ a nanoscale transport probe to study such complex correlation across an interface between $SrRuO_3$ on semiconducting Nb:$SrTiO_3$ (Nb:STO). Principally, this technique allows us to study any material system, whose electronic properties are susceptible to a temperature driven phase transition, while simultaneously allowing us to investigate its homogeneity across such buried interfaces with a semiconductor, at the nanoscale. This is an important approach for material systems such as complex oxides where small changes in the geometrical properties with thickness or temperature can produce large changes in the electric and magnetic properties. We perform a systematic experimental study to understand the effect of thickness and temperature on electronic transport across thin films of $SrRuO_3$ with Nb:STO and observe an order of magnitude increase in the transmission in the same device, across its ferromagnetic phase transition. Surprisingly though, we find that this increase originates from an enhanced transmission at the interface between $SrRuO_3$ and Nb:$SrTiO_3$, rather than in the bulk of $SrRuO_3$, and manifests as two different transport lengths at room temperature and below T_C=160 K[126]. We combine these findings with density functional theory calculations to quantitatively understand the role of interface reconstruction, octahedral distortions and exchange splitting to the electronic band structure of $SrRuO_3$ thin films and to electronic transport.

1. Thickness and temperature dependent BEEM transmission

High quality films of $SrRuO_3$ were grown varying the thickness d_{SrRuO_3}=6, 8, 9 and 10 unit cells (u.c.) on Nb:STO substrates. Our experimental nanoscale transport probe is known as ballistic electron emission microscopy (BEEM) which uses the scanning tunneling microscope (STM) to inject a distribution of hot electrons with energies higher than at the Fermi energy (E_F). An electrical contact between the STM tip and $SrRuO_3$ measures the tunnel current. These injected hot-electrons travel across the metallic base to reach the metal-semiconductor (M-S) interface; if their energy is sufficient to overcome the Schottky barrier, they can be collected into the semiconductor conduction bands.[123] As these hot electrons propagate through the $SrRuO_3$ thin films, they undergo scattering which influences the collected current.

The hot electron distribution encounters elastic and inelastic scattering while transmitting through the $SrRuO_3$ metallic base. In this process, the momentum distribution at the M-S interface is broadened, as compared to the injection interface, adding to the reduction of the collected BEEM current (I_B)[127]. These effects get more pronounced as the thickness of the base layer is increased. The normalized BEEM transmission follows an exponential behavior as described by[128]:

$$\frac{I_B}{I_T} = C \times exp\left[-\frac{d_{SrRuO_3}}{\lambda_{SrRuO_3}(E)}\right] \tag{2}$$

where $\lambda_{SrRuO_3}(E)$ is the energy-dependent hot electron attenuation length, I_B is the collected BEEM current, I_T is the injected tunnel current and C is a constant that is the kinematic transmission factor representative of electron transport across the M-S interface. The transmission for all film thicknesses is low up to a certain bias voltage beyond which, the transmission increases rapidly. This onset in bias voltage corresponds to the local Schottky barrier height (SBH) at the M-S interface. The value of SBH in the paramagnetic case is 1.13±0.03 eV[129]. It matches well with our previously extracted values for such an interface[130]. As the thickness of $SrRuO_3$ films is increased, the local SBH extracted from measurements on films of different thicknesses are found to be the same.

Electronic transport across the ferromagnetic phase transition in $SrRuO_3$ thin films was studied across its interface with Nb:STO, in the same set of devices, by performing similar BEEM measurements at 120 K. Similar to our earlier observations, the BEEM transmission progressively decreases with increasing thickness of the films. We find that the hot electron transmission increases by an order of magnitude as compared to its corresponding values at 300 K. The extracted SBH at 120 K, at these interfaces, is found to be 1.14 eV, which is the same as that obtained in its paramagnetic phase. One can thus safely discard the origin of the enhanced BEEM transmission in $SrRuO_3$ at 120 K, due to differences in the SBH across its magnetic phase transition.

2. Influence of interface and film thickness on electronic transport.

An exponential fit of the energy dependence of BEEM transmission for varying thickness of $SrRuO_3$ films allows us to extract the (energy dependent) transport length scale known as attenuation length (Equation 2). Above E_F,

the transmission of hot electrons in $SrRuO_3$ films is mostly governed by inelastic scattering, originating from the availability of increased phase space for hot electrons to decay into[131,132]. The extracted attenuation length of the carriers reflects the combined effects of inelastic, elastic as well as quasi-elastic scatterings. Extrapolation of the data for zero $SrRuO_3$ thickness shows two orders higher transmission, at the interface for ferromagnetic $SrRuO_3$. Such an enhanced interface transmission has not been earlier observed in other metallic systems using BEEM. An exponential fit using Equation 2, yields an attenuation length of 1.6 u.c. in the paramagnetic phase and 0.88 u.c. in the ferromagnetic phase. We find that the attenuation length slightly decreases with increasing energy, consistent with the enhancement of the density of states (DOS) at higher energies. What is surprising is that in-spite of the enhanced transmission in the ferromagnetic phase, the attenuation length in $SrRuO_3$ is shorter, for all energies at 120 K, than at RT. This apparent conundrum is explained by our *ab-initio* calculations, taking into account the characteristics of geometries and electronic structures at the interface between $SrRuO_3$ and $SrTiO_3$ along with the quasiparticle renormalization of attenuation length.

3. Ab-initio study of $SrRuO_3/SrTiO_3$(001) interfaces

We have performed *ab-initio* density functional calculations with a specific focus on correlating the structural and electronic properties at the interface to the BEEM transmission and to understand the origin of the flipping of the attenuation lengths at 120 K and RT. In order to simulate $SrRuO_3$ thin films grown on $SrTiO_3$ (001) substrates, we fix the lattice parameter a to the experimental value of the $SrTiO_3$ substrate. 3, 6 and 9 unit cells of $SrRuO_3$ have been considered in the low temperature ferromagnetic and room temperature paramagnetic phases. As a paramagnetic phase with disordered local moments is difficult to simulate within our computational technique, we study the nonmagnetic phase as the RT phase and ferromagnetic phase calculated at 0 K will represent the LT (low temperature) phase. We show in Fig. 6 the supercell with 6 layers of $SrRuO_3$ on 3 layers of $SrTiO_3$. In the following discussions, we will follow the notation shown in Fig. 6, where we denote STOL (or SROL) with L=1,2,..., the L-th layer from the $SrTiO_3/SrRuO_3$ interface.

4. Variation of the electronic and structural properties of the interface at LT and RT

To understand the experimentally observed enhancement in the interface transmissions at 120 K and RT, we calculate the electronic and geometric structures of $SrRuO_3/SrTiO_3$ interfaces. Looking at the geometric and magnetic properties, we can divide the $SrRuO_3$ thin films in three regions along the c-axis: surface, inner layer and interface region. Our calculated densities of states of $SrRuO_3$ along with that of $SrTiO_3$ are shown in Fig. 7-(a) for 9 u.c. of $SrRuO_3$ in the LT ferromagnetic phase and the RT nonmagnetic phases. It is observed that between 1 eV and 2.2 eV, the DOS in $SrRuO_3$ is dominated by e_g electrons whereas in $SrTiO_3$, the t_{2g} electrons dominate with a larger DOS between 1.2 and 1.4 eV in the nonmagnetic phase of $SrRuO_3$. The exchange split e_g state produces a smaller DOS at LT between 1.2 and 1.4 eV. While we observe the differences between LT and RT phases in all SRO layers, SRO1 layer at the interface needs an extra attention. A distinct feature of $d_{x^2-y^2}$ character (marked by the shaded area) is observed for RT phase in the SRO1 layer along with the renormalization of e_g DOS between 1.2 and 1.3 eV. Our calculated hopping parameters, for example, for the 6 u.c. at RT are 580 meV between the x^2-y^2 orbitals (corresponding Wannier function shown in Fig. 6 in the SRO1 layer and 540-543 meV for other layers. Also, the hopping mismatch between interface (575 meV) and inner layers (554-561 meV) is reduced at LT. Thus, we can clearly state that the mismatch between interface and inner layers is larger at RT. We further note from our DOS calculations that the mismatch of the electronic states at the interface between $SrRuO_3$ and $SrTiO_3$ is larger at RT than at LT. Such elastic scattering effects will lead to a reduction in the BEEM transmission at RT. All these differences in the electronic structures of the two phases strongly suggest the importance of the kinematic transmission factor C in Equation (2), which influences the BEEM transmission at LT and RT phases.

The difference in the characteristics at the interface for LT and RT phases is quite evident also in the structural properties, which is shown in Fig. 7-(b). For a slab of reasonable thickness (9 u.c. in our case), one can quantitatively identify the surface, inner layers and interface regions by the evolution of the Ru-O-Ru bond angle in the *ab* plane along the c-axis as shown in Fig. 7-(b). For the 9 u.c. case, a large region of inner layers (properties similar to bulk) exists while this region is not distinctly observed in the 3 u.c. case. Due to the interface reconstruction, the interface layer SRO1 is characterized by a Ru-O-Ru in plane bond angle having a value between the $SrRuO_3$ and $SrTiO_3$ bulk values. The properties of the inner layers are closer to the bulk. At the surface, we always obtain a bond angle larger

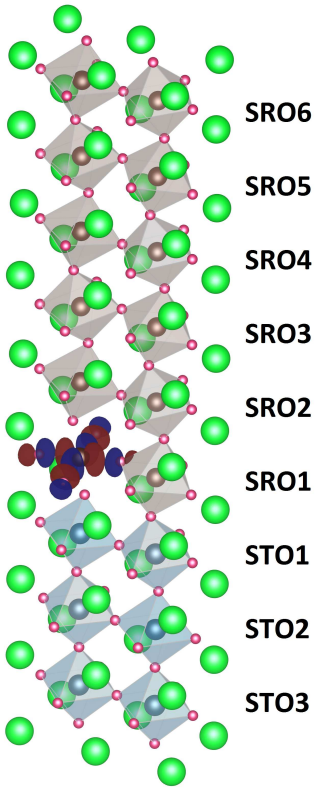

FIG. 6: Side view of the slab and calculated attenuation length. (a) Side view of the slab with 3 layers of $SrTiO_3$ and 6 layers of $SrRuO_3$. Sr, O, Ru and Ti atoms are shown as green, fuchsia, grey and blue balls respectively. In the SRO1 layer, we show the Wannier function corresponding to the x^2-y^2 orbital where red and blue contours are for isosurfaces of identical absolute values but opposite signs.

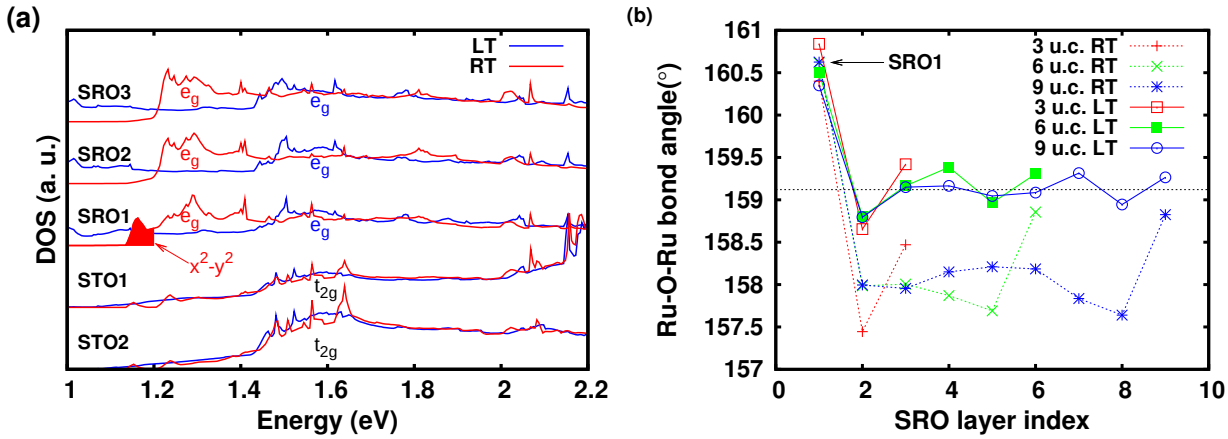

FIG. 7: Electronic and structural mismatch at the interface. (a) Layer projected DOS (spin-up + spin-down) closer to the interface from STO2 to SRO_3 for the 9 u.c. case. The LT (RT) phase is shown in blue (red). The shaded DOS below 1.2 eV in the RT SRO1 layer has x^2-y^2 character. The energy range is from 1.0 eV to 2.2 eV. (b) Ru-O-Ru bond angle in the *ab* plane as a function of the layer index for LT (solid lines) and RT (dashed lines) phases. The red, green and blue lines represent respectively the 3 u.c., 6 u.c. and 9 u.c. cases. The black dashed line represents the calculated LT bulk value in the same volume setup. The SRO1 layer values are indicated by the arrow.

than the bulk. Apart from the general differences between bond angles for different regions of the slab, an important observation can be made regarding the bond angles for the LT and RT phases.

It is clearly seen that the difference in bond angle between SRO1 and other SRO layers is larger for the RT phase compared to the LT one. For example, in the 6 u.c. case, the difference in the bond angle between SRO1 and SRO5

is 1.5° for the LT phase, while it is 3.0° for the RT phase (Fig. 7-(b)). This influences the hopping of electrons (as evident from the calculated hopping parameters mentioned above) and hence the transport properties at the interfaces and the kinematic transmission factor. Therefore, we can conclude that the differences in the geometries and electronic structures between SRO1 and other SRO layers are less dramatic in the LT phase compared to the RT one, which may effectively lead to an enhanced transmission of hot electrons across the interface at LT. The larger mismatch at RT between interface and inner layers will yield the kinematic transmission factor (C factor in Equation (2)) smaller for the RT phase. Such a substantial influence of geometric and structural changes at the interface leading to strong temperature dependent transport characteristics across the magnetic phase transition in $SrRuO_3$ is a remarkable finding, not observed before in any oxide heterostructure.

C. Summary of the ruthenates interface

We determined how the interface changes the structural and electronic properties of different configurations of ruthenates superlattices. In the Sr_2RuO_4-$Sr_3Ru_2O_7$, the shift of the atoms and the octahedral rotations change the VHS position affecting the DOS and the properties of the collective modes, while in the $SrRuO_3$/$SrTiO_3$ the interplay between octahedral distortions, bandwidth and magnetism produces different kinematic transmission factors across the interface.

More in detail, we have shown that, due to the different symmetry and size of the n=1 and n=2 elements, a rearrangement of the atomic position takes place both within the RuO_2 and SrO layers. The RuO_6 octahedra at the Sr_2RuO_4-$Sr_3Ru_2O_7$ interface get elongated in the Sr_2RuO_4 side and flattened in the $Sr_3Ru_2O_7$ along the c-axis when compared to the octahedra in the inner layers. Another interesting feature is the observation of the change of misalignment of Sr atoms with respect to the O atoms in the SrO blocks at the Sr_2RuO_4-$Sr_3Ru_2O_7$ interface. This influences the Ru-O-Ru bond angle resulting into a less pronounced rotation of the $Sr_3Ru_2O_7$ octahedra and a displacement of the Ru atom with respect to the oxygen plane in the Sr_2RuO_4 side of the interface. Concerning the electronic structure, we find out that the superlattice electronic parameters are quite uniform and exhibit small differences between the interface and inner Ru bands. Furthermore, the symmetry allowed hopping in the superlattice are analogue to those in the Sr_2RuO_4 and $Sr_3Ru_2O_7$ bulk phases with the major changes occurring in the modification of the amplitude of the electronic processes.

We have studied the BEEM transmission through thin films of $SrRuO_3$ of various thicknesses, interfaced with $SrTiO_3$ across its magnetic transition. The increase in BEEM transmission at 120 K compared to RT is accompanied by a surprising flipping of the attenuation length. Our first principles calculations indicate strong geometrical reconstructions at the interfaces characterized by Ru-O-Ru bond angles along with distinct features in electronic structures of the Ru-d orbitals, both of which are strongly dependent on the magnetic phases. As a consequence, the importance of the transmission factor is realized to explain the experimentally observed BEEM transmission data. Moreover, the inclusion of the temperature dependent quasiparticle weight for the calculation of the attenuation length correctly describes the experimental observation at 120 K and RT.

V. VERTICAL SHIFT AT THE OXIDES INTERFACE

Exchange bias is one such outcome of interfacial coupling across two different magnetic states,[133] usually antiferromagnetic and ferromagnetic phases. In perovskite based heterostructures, magnetic interactions are particularly fascinating as they can show interface ferromagnetism between two antiferromagnets or between an antiferromagnet and a paramagnet.[134] Competing magnetic interactions, which give rise to proximity coupling such as exchange bias have found technological applications in magnetoresistive sensors, however its microscopic origin often raises debates particularly regarding the coupling configurations at the interface.[133]

Orthorhombic $YMnO_3$ is a ferroelectric antiferromagnet with T_{FE}≈30 K and T_N≈42 K. The reported ferroelectric properties of $YMnO_3$ thin films indicate the occurrence of the coexistence of cycloidal and E-type antiferromagnetic orderings[135] or of commensurate E-type antiferromagnetic ordering at low temperatures.[136] Orthorhombic $YMnO_3$ is also energetically close to antiferomagnetic A-type ordering.[137] Since the magnetic properties of $YMnO_3$ lie at the verge between different magnetic orderings, it is tempting to speculate that interfaces could modify this ordering as well the electronic and structural properties.

Magnetic heterostructures showing a horizontal shift of hysteresis loop along the field axis have been commonly observed for bilayer combinations.[117,138] However, an uncommonly observed effect of exchange coupling across an AFM/FM interface is the shift along the magnetization axis or the vertical shift.[139] Element specific magnetic studies with X-rays of FeF_2/Co and CoO/Fe[140,141] layered structures confirmed the existence of this vertical shift and

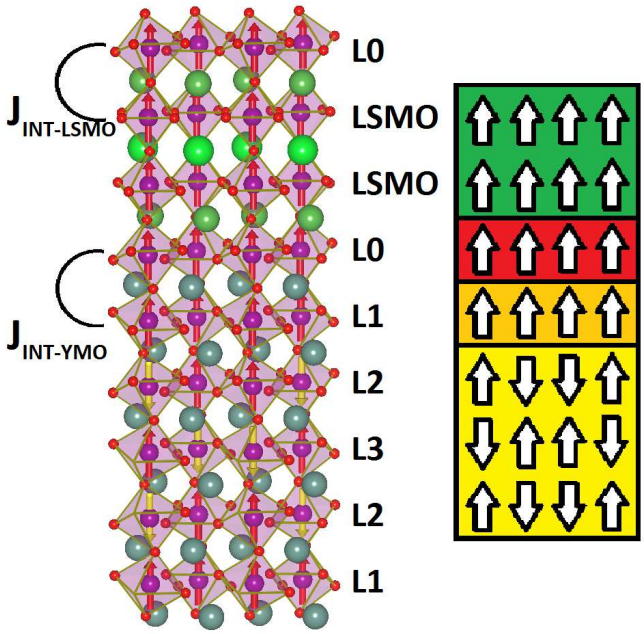

FIG. 8: Ground state geometry and magnetic structure of LSMO/YMO heterostructure with 5 $YMnO_3$ layers (left) and the corresponding schematic picture showing different regions and their magnetic configurations (right). MnO_6 octahedra are shown with red (yellow) arrows indicating up (down) moments on Mn atoms. For simplicity, we do not show the direction of the moment in the *ab* plane. Y, La and Sr atoms are shown as dark blue, dark green and light green balls. $J_{INT-YMO}$ ($J_{INT-LSMO}$) is the effective magnetic superexchange along the *c* axis between interface Mn atoms and Mn atoms of L1 (LSMO) layer.

revealed its relation to specific uncompensated moments in the antiferromagnet. The vertical shift is the irreversible magnetization of the non ferromagnetic layer[142] and it was conjectured to be either correlated or not correlated to the bias field, but no convincing experiment could be made possible to identify due to the extremely small magnitude of the vertical shift. However, a study on heteroepitaxial interfaces involving $YMnO_3$ and the weak anisotropic ferromagnet $La_{0.7}Sr_{0.3}MnO_3$ (LSMO) showed an unusually large vertical shift. It was also shown that this vertical shift was correlated with the horizontal shift.[143,144] Samples with a larger horizontal shift showed a smaller vertical shift and vice versa as in other systems.[145]. In core/shell structured Fe nanoparticles, large exchange bias and vertical shifts were attributed to the frozen moments in a spin-glass like phase in the shell of the nanoparticles.[146] However the horizontal shift in $YMnO_3/La_{0.7}Sr_{0.3}MnO_3$ is negligible compared with the vertical shift. The vertical shift was found together with the horizontal shift,[147,148] but this system basically shows a pure vertical shift in the hysteresis loop. $YMnO_3/La_{2/3}Sr_{1/3}MnO_3$ heterostructure is the missing element in the phenomenology of the magnetic interface and can be a key point in the understanding of the magnetic interface phenomena. In this Section, we focus on the coupling between AFM $YMnO_3$ and FM $La_{2/3}Sr_{1/3}MnO_3$[149] to understand what is the specificity of this system to create a pure vertical shift. More results are reported in the paper p2.

A. First principles calculations of the $YMnO_3/La_{0.7}Sr_{0.3}MnO_3$ heterostructures-p2

First, we study the case of a heterostrusture with 2 $YMnO_3$ layers, 2 LSMO layers and 2 interface layers from structural and magnetic point of view. Further, using the results of this heterostructure, we analyze in more detail the properties of a larger supercell with 5 $YMnO_3$ layers.

1. Superlattice: structural properties

We have used the experimental values[136] of $YMnO_3$ for the in-plane lattice parameters of the supercell. For the *c* axis, the bulk value has been chosen and at the interface, the average out-of-plane separation between $YMnO_3$ and LSMO has been used to get the total *c* value of the supercell. The following notations will be used for the heterostructure, we define L0 as the interface layer and L1 as the first neighbor layer. In the supercell with 5 $YMnO_3$

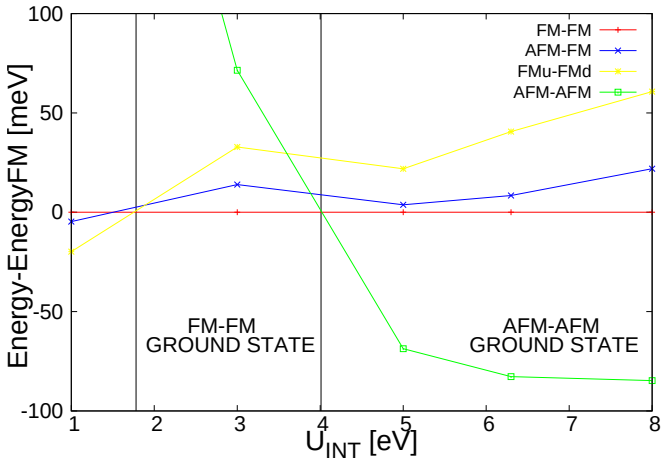

FIG. 9: Total energies of the magnetic phases of $YMnO_3$/LSMO with 6 layers as a function of Coulomb repulsion at the interface. We report the difference between one magnetic phase and the fully ferromagnetic solution. The fully ferromagnetic solution is the ground state between 1.8 and 4.0 eV.

layers, the second and third neighbor layers of the interface are denoted as L2 and L3 respectively, as shown in Fig. 8.

First of all, we study the smaller supercell with 2 $YMnO_3$ layers. In our interface model, we have a layer of YO, a layer of MnO_2 and another layer of $La_{1-x}Sr_xO$ that close the cage around the MnO_6 octahedra. However, the exact stoichiometry of the $La_{1-x}Sr_xO$ layer at the interface is unknown. We have calculated the energies for different magnetic phases and different Coulomb repulsion parameters U_{INT} (Coulomb repulsion for the interface). The most stable configuration is with LaO layers and SrO layers in agreement with similar results for other kinds of supercells[150,151] and the interface with only La atoms has always the lowest energy. Therefore, at the interface, we have MnO_6 octahedra enclosed in a cage with Y on one side and La on the other side. Probably, the La atoms are energetically favored because of their atomic radii being very similar to the Y radii. As Y and La are electronically equivalent, there is no charge doping or double exchange at the interface. Thus the interface layer can be metallic or insulator depending on the magnetic phase. On the other hand, the inner layers of LSMO will be always metallic because of the presence of Sr that produces a charge doping.

Assuming the LaO layer at the interface, we report the results for the supercell with 5 $YMnO_3$ layers at U_{INT}=2 eV and U_{INN}=3 eV with the magnetic ground state reported in Fig. 8, where U_{INN} is the Coulomb repulsion for the interface. The magnetic ground state, discussed in the next subsection, is composed of ferromagnetic layers at the interface (L0) and the first layer of $YMnO_3$ (L1). We find that the structural properties of the interface layer L0 are intermediate between $YMnO_3$ and LSMO.

2. Superlattice: magnetic properties

Besides the most stable magnetic phases, *G*-type, *A*-type and *E*-type magnetic phases were also studied at the interface. The spin configuration is $3d^4\uparrow$ according to Hund's rule both for the interface and $YMnO_3$ inner layers independently from the magnetic phase, while it is $3d^{3.5}\uparrow$ in the LSMO due to the charge doping. We report the energy as function of U_{INT} in Fig. 9 for different magnetic phases. The four following magnetic phases are close to the ground state:

1. a fully ferromagnetic phase (FM-FM)
2. an antiferromagnetic *E*-type in $YMnO_3$ and ferromagnetic phase in LSMO and interface (AFM-FM)
3. a ferromagnetic phase with spin up in $YMnO_3$ and a ferromagnetic with spin down in LSMO and interface (FMu-FMd)
4. an antiferromagnetic *E*-type in $YMnO_3$ and an antiferromagnetic *A*-type in LSMO and interface (AFM-AFM)

We find that in the range of typical U_{INT} for this system (between 1.8 and 4.1 eV) the heterostructure is completely ferromagnetic also in $YMnO_3$. Above 4.1 eV, we find an *E*-type solution in $YMnO_3$ and an *A*-type solution in LSMO.

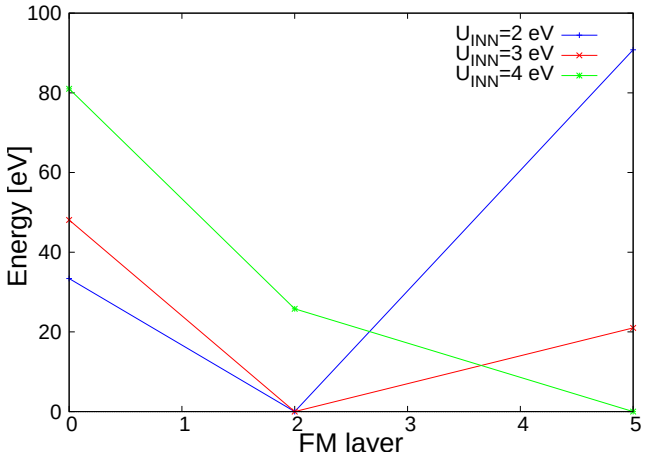

FIG. 10: Total energy as a function of the number of ferromagnetic $YMnO_3$ layers for the heterostructure with 5 $YMnO_3$ layers. The energy of the ground state is set to zero. In the configuration with no FM layers, we have 5 E-type AFM layers. In the configuration with 2 FM layers, we have two ferromagnetic L1 layers. In the configuration with 5 FM layers, the heterostructure is fully ferromagnetic.

We remember that the heterostructure is orthorhombic. Instead, the LSMO bulk system is pseudocubic and does not present any instability towards the A-type magnetic order. Finally, at very low values of U_{INT}, we have the ferromagnetic $YMnO_3$ with opposite moments with respect to the ferromagnetic LSMO and interface. Remarkably, AFM E-type in $YMnO_3$ and FM LSMO and interface is the sum of the two bulk ground states, however is never the ground state. Although U_{INT} is a local property of the interface layer, we can see that it influences the properties of the whole heterostructure determining a change of the magnetic properties. A small variation of U_{INT} can also have long range effects on the magnetic properties.

When we analyze the bigger supercell with 5 $YMnO_3$ layers we have qualitatively similar results. To investigate how the ferromagnetism goes deep in the $YMnO_3$ region, we analyze the magnetic properties as function of U_{INN} in Fig. 10. Two ferromagnetic layers for U_{INN}=2-3 eV are present in the ground state. These two ferromagnetic layers correspond to the two L1 layers in Fig. 8. When U_{INN}=4 eV all the 5 $YMnO_3$ layers become ferromagnetic. In summary, we found in two different supercells and in the typical range of Coulomb repulsion for this system that the first neighbor layer of the interface is ferromagnetic. This is in agrement with observed few nanometers of ferromagnetic layer at the interface of $YMnO_3$/LSMO.[144] The $YMnO_3$ develops an interface-induced ferromagnetism as in other perovskite systems at the borderline between different magnetic orders[117,152]. We also calculate the superexchange parameters for the supercell with 5 $YMnO_3$ layer and we get $J_{INT-LSMO}$=-39 meV, therefore there is a strong coupling between the interface and LSMO. Instead, the coupling $J_{INT-YMO}$ between L0 and L1 is just -1.2 meV. Moreover, we propose the following argument to additionally support our conclusions. We will show that the $YMnO_3$ ferromagnetic phase has larger bandwidth respect to the antiferromagnetic phase. The LSMO phase also has large bandwidth and can hybridize the $YMnO_3$ increasing its bandwidth and favoring its ferromagnetic phase.

3. Superlattice: electronic properties

We calculated the DOS for the heterostructure shown in Fig. 11. As expected, the LSMO region shows a metallic behavior (Fig. 11-(a)). In the L0 layer we have 3 electrons in the t_{2g} manifold and one occupied electron in the e_g. There are two e_g metallic bands at the Fermi level in the L0 layer (Fig. 11-(b)). Remarkably, the most occupied e_g orbital is x^2-y^2 as shown in Fig. 12 though the layer is metallic and also the $3z^2$-r^2 orbital gives us a strong contribution to the DOS at the Fermi level. However, this is completely different from $YMnO_3$ where the most occupied orbital has $3l^2$-r^2 (l=long bond) character in the bulk and heterostructure in both FM and AFM phases. The interface layer is half metallic while both the FM and AFM $YMnO_3$ layers are insulators as observed in the local DOS of these atoms respectively in Fig. 11-(c) and Fig. 11-(d). Electrons on atoms with spin majority down are more localized and the bandwidth is narrower in the DOS.

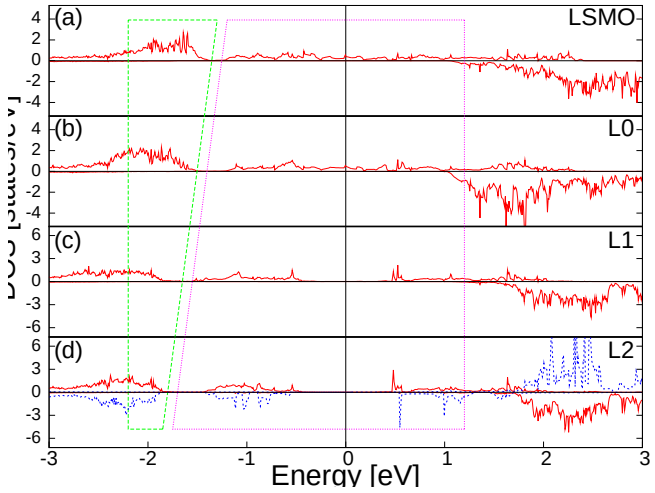

FIG. 11: Layer-resolved DOS of the superlattice with 5 $YMnO_3$ layers. The Fermi energy is set to zero. Spin up (down) contribution are shown in the positive (negative) y-axis. The (a), (b), (c), (d) panel show respectively the local DOS of Mn atoms in the LSMO, L0, L1 and L2 layer. The DOS of the L3 layer is very similar to L2. The entire system shows a half-metallic behavior. Solid red (dashed blue) line represents the DOS of the Mn atoms where the spin majority is up (down). We indicate in the Figure the region where the main orbital contribution to the DOS for the majority spin is t_{2g} (green dashed line) and e_g (pink dotted line).

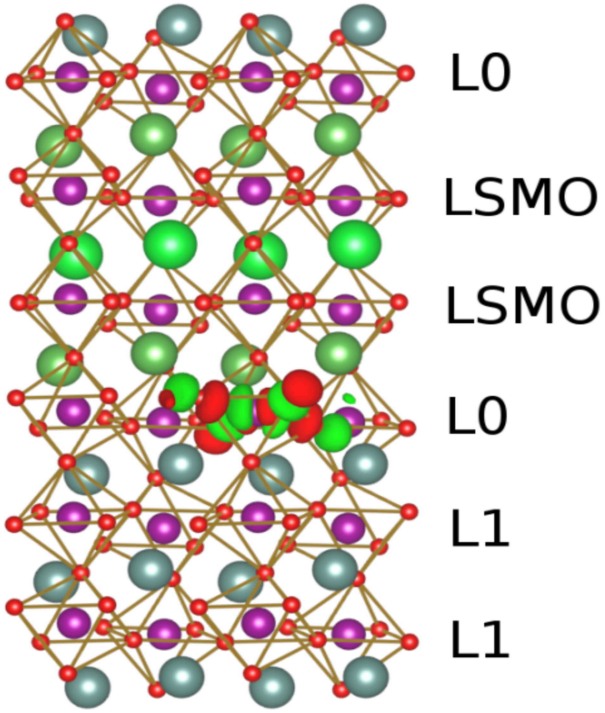

FIG. 12: Occupied e_g-like Wannier state on Mn atoms at the interface for the heterostructure with 2 $YMnO_3$ layers. The orbital is of x^2-y^2 nature.

B. Bulk $YMnO_3$

We have reported an unusual FM phase in $YMnO_3$ in the previous section. To understand more about this new phase, we study and compare the FM and AFM phases at the experimental volume. Let us consider three pseudocubic axes along the Mn-Mn directions for $YMnO_3$. There are 3 inequivalent directions for $YMnO_3$, which are called 1, 2 and c. Along the direction 1, the coupling is ferromagnetic while along the directions 2 and c, it is antiferromagnetic.

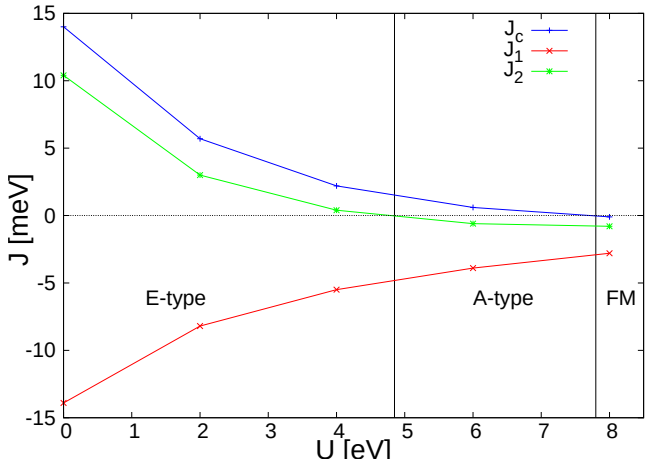

FIG. 13: Effective superexchange for $YMnO_3$ at experimental positions as function of U. We have three independent value of J. If J is negative we have FM coupling, if J is positive we have AFM coupling. When J_1 is negative and the others are positive we have the E-type magnetism. When J_1 and J_2 are negative and J_c is positive we have the A-type magnetism. Finally, when they are all negative we have the FM phase.

1. *Magnetic and structural phases*

We can map our $YMnO_3$ system in a Heisenberg model:

$$H = \sum_{<i,j>} J_{i,j} S_i \cdot S_j \tag{3}$$

where the sum is over pairs of adjacent spins. We report in Fig. 13 the values of magnetic superexchange $J_{i,j}$ as function of U and with a fixed ratio between the Hund coupling and Coulomb repulsion J_H/U=0.15. Depending on the U value, we have 3 magnetic phases: E-type at low U, A-type at intermediate U and FM at high U. The results are in agreement with Ref. 153. The experimental magnetic phase is reproduced for U <4 eV. The ferromagnetic phase of $YMnO_3$ has the same group symmetry of the dielectric phase ($Pbnm$). In this new phase, we recover the inversion symmetry.

Electrons are more localized in the AFM E-type phase than in the FM phase. JT is reduced in the FM phase and (l-s)/(l+s) goes from 0.077 in the E-type to 0.067 in the FM phase. The orbital order is $3l^2$-r^2 in both magnetic phases and also hopping parameters are not modified.

2. *Hopping parameters*

The low-energy physics of $YMnO_3$ can be captured by e_g states. We calculate the hopping parameters for the low energy band structure in the basis of e_g-like Wannier functions. The hopping parameters of the nonmagnetic phase for the e_g manifold are reported in Table V. The hopping in the ab plane are almost similar, small differences rise from different bond angles and Mn-Mn distances. In a perfect tetragonal symmetry, we should find $|t^{1,2}_{p,q}|$ along the direction 1 equal to $|t^{1,2}_{q,p}|$ along the direction 2. We find a large hopping $t^{1,2}_{p,p}$=-243-4 meV between x^2-y^2-like Wannier function in the ab plane, and we have a hopping between $3z^2$-r^2-like Wannier function along the c direction that is -307 meV. These values of hoppings are in good agreement with values for other Mn-perovskites. We observe that the second neighbor hopping are strongly asymmetric along the two directions a and b. It was shown that the orbital order is $3l^2$-r^2 and considering the larger value of b, the charge of the Mn atoms points towards the direction b. This is the main reason why the hopping parameters are bigger along the b-axis creating a large anisotropy in the plane.

3. *Electronic properties*

We investigate the electronic properties of the AFM and FM phases of bulk $YMnO_3$. We show the influence of the Jahn-Teller effect and the change of symmetry on the DOS in the FM phase. Both magnetic phases show insulating

TABLE V: Hopping parameters in $YMnO_3$ in the e_g-like basis at experimental positions. The basis is composed by $|x^2-y^2,1\rangle$, $|x^2-y^2,2\rangle$, $|3z^2-r^2,1\rangle$ and $|3z^2-r^2,2\rangle$. Hopping integrals $t^{i,i'}_{j,j'}$ are from a site i with orbital j to neighboring site i' with orbital j'. The connecting vector is $\mathbf{T} = l\mathbf{x} + m\mathbf{y} + n\mathbf{z}$ where the vectors $\mathbf{x}$, $\mathbf{y}$ and $\mathbf{z}$ connect two first-neighbor Mn atoms first-neighbor; the hopping integrals are tabulated up to the first-neighbor. ϵ^i_j is the energy on site for the orbital j on the site i and Δ^i is the on-site interorbital hopping of the atom i. We denote p and q respectively the orbitals x^2-y^2 and $3z^2$-r^2 in the hopping notation. We also report second neighbor hopping parameters along the two strongly different a and b axes. All energies are in meV.

	ε_p	ε_q	Δ^1	Δ^2
	1591	2019	438	438
	First Neighbor			
Direction	$t^{1,2}_{p,p}$	$t^{1,2}_{p,q}$	$t^{1,2}_{q,p}$	$t^{1,2}_{q,q}$
1	-243	203	137	-109
2	-244	-138	-203	-112
c	-53	-79	-79	-307
	Second Neighbor			
Direction	$t^{1,2}_{p,p}$	$t^{1,2}_{p,q}$	$t^{1,2}_{q,p}$	$t^{1,2}_{q,q}$
a	16	6	5	-6
b	59	3	4	-28

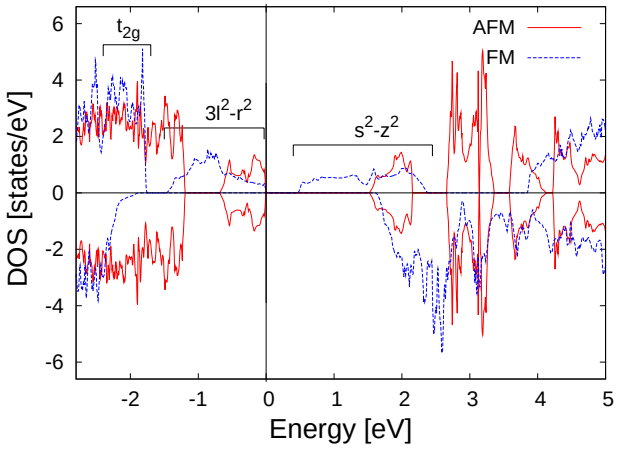

FIG. 14: Total DOS per formula unit for $YMnO_3$ in the E-type (red solid line) and FM (blue dashed line) phase. The Fermi level is set to zero. Majority (minority) spin contribution are shown in the positive (negative) y-axis. We indicate in the Figure the main orbital contribution to the DOS for the majority spin of the FM phase.

behavior (see Fig. 14). In the AFM case we have the t_{2g} at 1 eV below the Fermi level, while in the FM case is as 2 eV below the Fermi level. Instead of the classical e_g orbital, we have a linear combination of them. In both magnetic phases, we have the orbitals $3l^2$-r^2 just below the Fermi level and the s^2-z^2 just above the Fermi level as already known[154] for the AFM phase. In the FM case, the bandwidth is larger because electrons are more delocalized.

4. Magnetocrystalline anisotropy

As the magnetic field in the experimental case is applied in the ab plane, we are interested to study the anisotropy for the same situation. For the ferromagnetic $Pbnm$ phase, the formula for the anisotropy energy E_A in the ab plane

for this system is

$$E_A(\phi) = K_2 \cos^2 \phi + K_4 \cos^4 \phi \tag{4}$$

where ϕ is the angle between the a-axis and the magnetization in the ab plane. As the hard axis is along the c-axis, we can neglect it in the expression (4) for anisotropy energy. Our calculated *ab-initio* value of the magnetocrystalline anisotropy in the ferromagnetic phase is K_2=0.561 meV[144] per formula unit for the leading term. The higher order anisotropy term K_4 is also reported in Table VI and is found to be negligible. As the value of K_2 is positive, the easy axis is along the b axis when ϕ=90°. Our calculated value of K_2 is quite big in comparison to the values found in the literature[155] and is also two orders of magnitude greater than usual magnetocrystalline constants. This large value originates from a significant anisotropy b/a=1.111 between the lattice parameters combined with the $3l^2$-r^2 orbital order.

TABLE VI: Magnetocrystalline anisotropy constants for $YMnO_3$ in a fully ferromagnetic bulk phase.

	K_2	K_4
meV/(formula unit)	0.561	0.008
10^4 J/m^3=10^5 erg/cm^3	160	2

To simulate the hysteresis we need to take into account the interaction of the magnetic system with the external magnetic field. The effect of the magnetic field on the energy is represented by the Zeeman energy E_H, which is expressed as:

$$E_H(\phi) = -MH \cos(\phi - \phi_F) \tag{5}$$

where ϕ_F is the direction of the external magnetic field H and $\phi - \phi_F$ is the angle between the magnetic field and the magnetic moment M. Here, we do not take into account interface and shape anisotropies. Our calculated total magnetic moment $\mathbf{M}$=$\mathbf{M_{spin}}$+$\mathbf{M_{orbital}}$ is M=3.62 μ_B per Mn atom. Adding the equations (4) and (5), we get the expression for the total energy as

$$E(\phi) = K_2 \cos^2 \phi - MH \cos(\phi - \phi_F). \tag{6}$$

For ϕ_F=90°, there is only one stable solution for H>H_C=$2K_2/M$ that is the coercive field in this limit case. In this simple model, this critical magnetic field coincides with the magnetic anisotropy field, that is the magnetic field needed to saturate the magnetization along the hard axis. Using the total energy (6) we calculate the hysteresis for $YMnO_3$. It is found that the coercive field H_C is of the order of 2-5×10^4 Oe, while in the experiment about $YMnO_3$/$La_{0.7}Sr_{0.3}MnO_3$ heterostructure[143] the magnetic field was up to 0.5×10^4 Oe. In our study, the magnetic anisotropy field is 5.4×10^4 Oe.

In LSMO, the expression for the magnetocrystalline anisotropy is

$$E(\theta) = K_2^{LSMO} \sin^2 \theta \tag{7}$$

where θ is the angle between the direction of the magnetization and the [001] direction. A very small anisotropy K_2^{LSMO}=0.18×10^4 J/m^3 was measured in LSMO[156]. Following equation (7), the easy axis is along the c axis and the hard axes are in the ab plane. However at the interface we have an orthorhombic structure of LSMO and hence we expect a small magnetocrystalline anisotropy with a different easy axis. However, we neglect this effect and consider the easy axes plane as the ab plane as suggested by the experiments.

C. Hysteresis loops for two independent ferromagnetic phases

In Ref. 143, a vertical shift m_{shift} in $YMnO_3$/$La_{0.7}Sr_{0.3}MnO_3$ heterostructures at 10 K was found experimentally and this vertical shift is attributed to the properties of the diluted antiferromagnetic state in a magnetic field. However, the properties of the diluted antiferromagnetic state disappears at low temperature in bulk $YMnO_3$ and an E-type AFM phase take place.[136] Instead, the nature of the large vertical shift might be found in the interdiffused ferromagnetic layer at the interface composed also by an unusual $YMnO_3$ ferromagnetic phase. We have shown that the $YMnO_3$ L1 layer near the interface becomes ferromagnetic. Therefore, the m_{shift} effect can be explained with the large coercivity

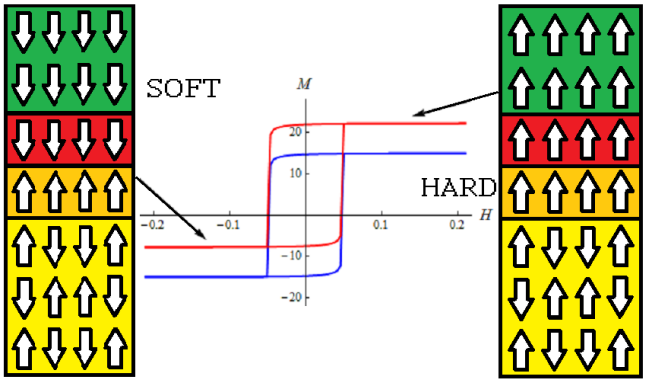

FIG. 15: Microscopic mechanism of pure vertical shift. The positive direction of the magnetic field is the direction of the field cooling. Magnetic configurations are shown with magnetic field in the positive (negative) direction on the right (left) side. The hard ferromagnetic layer (shown in orange) does not reverse its spin when a small magnetic field is applied in the negative direction. The results are obtained using ${K_2}^S = 0.002$ meV and show the hysteresis loop without hard ferromagnet (blue line) and with hard ferromagnet (red line). Schematic magnetic configurations are consistent with Fig. 8. The unit of external magnetic field is Tesla along the horizontal axis and arbitrary unit along the the vertical axis to represent magnetization.

of ferromagnetic $YMnO_3$. The magnetic field used to reverse the spin in ferromagnetic LSMO is too small to reverse the spin in ferromagnetic $YMnO_3$.

More clearly, the FM layer of $YMnO_3$ is a hard ferromagnet and weakly ferromagnetically coupled to the interface and LSMO. The region composed by the interface and LSMO is a soft ferromagnet. Let us assume that the ferromagnetic $YMnO_3$ is magnetically decoupled from the interface. The total energy of the system can be written in the following way:

$$E(\phi_S, \phi_H) \;=\; n_S(K_2^S \cos^2\phi_S - M^S H\cos(\phi_S - \phi_F)) + n_H(K_2^H \cos^2\phi_H - M^H H\cos(\phi_H - \phi_F)) \tag{8}$$

as the sum of the energy of a soft ferromagnet (S) and a hard ferromagnet (H). n_S and n_H represent respectively the numbers of atoms in the soft and hard ferromagnetic regions. When a relatively small magnetic field is applied, the hard ferromagnet does not reverse when the magnetic field is applied in the opposite direction, determining a shift of the magnetization. The magnetic configuration coming from equation (8) is shown in Fig. 15. The m_{shift} is the magnetization of the pinned magnetic moment in the AFM region. If we compare our results with the experimental values of the vertical shift, we observe that the FM phase of heterostructure should be composed of few interface layers of $YMnO_3$ within the approximation of a sharp interface. What seems to be important in the determination of m_{shift} is the roughness of the interface, which is not considered here. A large roughness give us a large ferromagnetic interdiffused layer and therefore a large m_{shift} as experimentally observed.[143] Another important condition is the weak coupling between the L0 and L1 layers, that permits the L0 layer to rotate avoiding to influence the L1 layer.

The peculiarity of this system is the weak exchange bias. The reduced horizontal shift arising from weak exchange bias can be attributed to the weak coupling between the rotating FM phase (L0) and the AFM phase (L2). Indeed, the exchange bias is proportional to the magnetic coupling between these phases.[157] However this is a second neighbor exchange interaction and hence, leads to a weak exchange bias. A large vertical shift comes from a large value of pinned magnetic moment in the AFM region and hence, the magnetic coupling between AFM and FM is weak. Large vertical shift is associated to a small exchange bias when the creation of the pinned magnetic moments destroys the antiferromagnetic order. To have the simultaneous presence of large magnetic moment and large exchange bias, we need a net magnetic moment in the AFM phase and an AFM phase strongly coupled to the FM phase. This is observed in other systems where the net magnetic moment is provided by non collinear magnetic structures in AFM phase or in a ferrimagnetic one[147,148].

This phenomenon of pure vertical shift is realized mainly due to three conditions. First, we need a FM layer in the AFM side of the interface. Second, this FM layer should have to be magnetically weakly coupled to the FM side of the interface. Finally, we need a large magnetocrystalline anisotropy of the FM layer relative to the FM side of the interface. The first two conditions are possible just when we have the A-type and the FM phases energetically close to the ground state as in the case of $YMnO_3$ (shown in Figs. 13). The third condition, that we need, is a strongly anisotropic system described above.

D. Summary of the vertical shift in $YMnO_3$/LSMO heterostructures

In conclusion, by means of first-principles density functional theory, we determined the structural, electronic and magnetic properties of $YMnO_3$/LSMO heterostructures. We find that the most stable structural configuration has a LaO layer in the LSMO side of the heterostructure. The interface layer shows half-metallic ferromagnetic behavior with the LSMO region of the superlattice and its DOS exhibiting a x^2-y^2 character at the Fermi level. Remarkably, it is found that this interface stabilizes an unusual insulating ferromagnetic phase in the layer closer to the interface in the $YMnO_3$ side. This unusual phase is only present at the interface of these two dissimilar oxides and is not found experimentally in the bulk.

The ferromagnetic phase of bulk $YMnO_3$ is insulating with a smaller band gap. It has a different space group (*Pbnm*) and a reduced Jahn-Teller effect compared to the usual bulk AFM phase. Moreover, our calculated hopping parameters in the *ab* plane are distinctly different along the *a* and the *b* axes yielding a strongly anisotropic ferromagnet with a large coercivity in the *ab* plane. Therefore, we have found a strongly anisotropic ferromagnet at the interface between an isotropic ferromagnet (LSMO) and a strongly anisotropic antiferromagnet ($YMnO_3$). We show that the magnetization within this ferromagnetic $YMnO_3$ layer is responsible for the large vertical shift observed in $YMnO_3$/LSMO heterostructures.[144]. Indeed, a relatively small magnetic field applied to the entire heterostructure can rotate the moments in the LSMO part while the moments in $YMnO_3$ are pinned due to large coercivity. This pinned magnetic moment in $YMnO_3$ causes the vertical shift m_{shift} in the hysteresis loop. Hence, one can conclude that the vertical shift is due to the net magnetization of the AFM layer.

The small value of the exchange bias in $YMnO_3$/LSMO is due to the magnetic profile where there is no first neighbor magnetic interaction between the rotating LSMO ferromagnetic region and the AFM inner layer region that produces the exchange bias. The existing weak second neighbor exchange interaction is tho weak to produce any significant exchange bias effects. Our conclusions support the idea that horizontal and vertical shifts observed in the hysteresis loops are correlated and tend to exclude each other if the creation of the pinned magnetic moments destroy the antiferromagnetic order. Thus our study, in general, would instigate revisits on various other systems showing such pure vertical shifts.

VI. INTERDIFFUSION OF OXYGEN AT THE INTERFACE

The possibility of combining metal oxides with metallic layers is fundamental not only for microelectronics, but also to provide a testbed for new physical phenomena, which may arise from the combination of functional oxides and metals. It is very well known, however, that the interfaces between reactive metals and oxides may become unstable, especially when exposed to high thermal load. Interestingly, interdiffusion can also lead to the formation of new interfacial phases, such as transition-metal oxides, which may exhibit novel properties[158–163]. Indeed, the oxygen interdiffusion plays a crucial role in the interface Fe/$BaTiO_3$. Depending on the migration of the O atoms at the interface, we can have the ferroelectric/ferromagnetic interface[161] or the Fe/FeO interface with new properties like the exchange-bias[162] not observed without the $BaTiO_3$.

In this Section, we focus on the Cr/$BaTiO_3$ system. $BaTiO_3$ (BTO) is a prototypical ferroelectric oxide with perovskite structure, widely employed for different applications, from magnetoelectric coupling with metals[161,164,165] and oxides[166], to electroresistive devices[167] even with memristive capabilities[168], to dedicated applications exploiting its piezoelectric, pyroelectric, and/or electro-optic properties[169]. Chromium is a highly reactive 3d metal, relatively abundant on earth[170], often used as an adhesion layer between noble metals and oxides for the realization of electrical contacts in microfabricated devices. Moreover, it is antiferromagnetic with a bulk Néel temperature of 311 K.

A. The defective phase of tetragonal chromium (III) oxide

In the reference **p6**, it was performed a systematic study of Cr ultrathin (1-2 nm) films, grown by molecular beam epitaxy and followed by annealing at different temperatures, on $BaTiO_3$ (001) underlayers. It was verified that the chromium oxide resulting from oxygen interdiffusion represents an uncommon tetragonal phase of Cr_2O_3, which gets stabilized by the epitaxy on BTO. We also discuss how, despite the different structural phase, the chemical and electronic properties of tetragonal chromium oxide are similar to those of bulk Cr_2O_3. We performed the calculations for U = 0, 3 and 6 eV, where the latter value is generally used for ionic correlated compounds presenting a reduced electron bandwidth like tetragonal Cr_2O_3. To prove that, we compare the t_{2g} bandwidth of the tetragonal Cr_2O_3 with other Cr-compounds with octahedral crystal field. Indeed, the tetragonal Cr_2O_3 shows a t_{2g} bandwidth of 2.5 eV that is small compared with the bandwidth of 3.5 eV for the CrAs[171] or the bandwidth of 5.0 eV for the elemental Cr[172]. To reproduce the defective rocksalt structure, we used a supercell where the lattice constants of the supercell

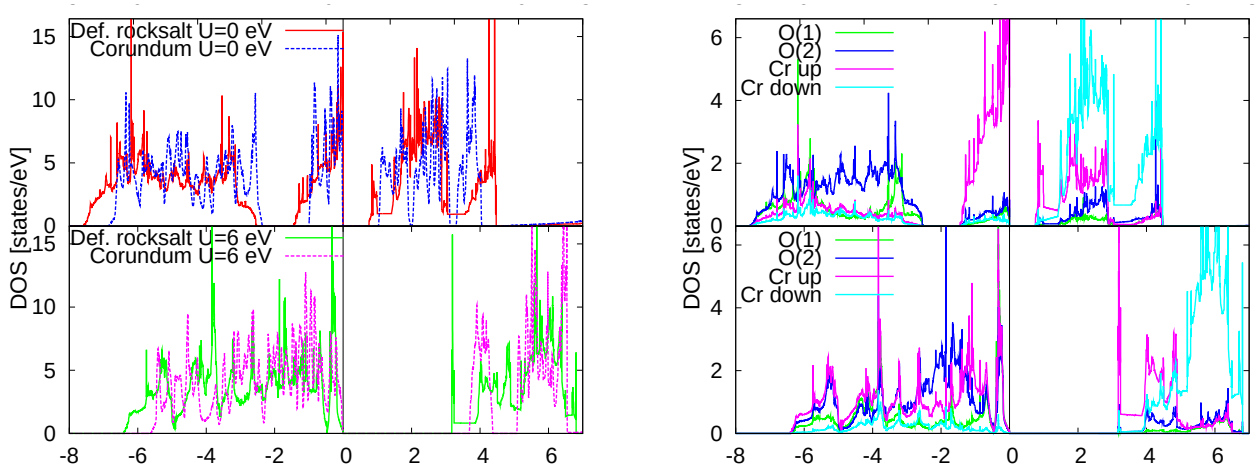

FIG. 16: Left panel: total electronic DOS for the defective rocksalt and corundum Cr_2O_3 at U=0 eV (top panel) and 6 eV (bottom panel). Right panel: electronic DOS projected on O(1), O(2), Cr up, and Cr down states for the defective rocksalt Cr_2O_3 at U=0 eV (top panel) and 6 eV (bottom panel). The Fermi level is set to zero.

are $a_{sup} = a/\sqrt{2}$, $b_{sup} = 3a_{sup}$, and $c_{sup} = c$. In this symmetry, the Cr atoms are equivalent, while there are two types of oxygens that we define O(1) and O(2). O(1) has 4 Cr nearest neighbor in the ab plane, while O(2) has 2 Cr nearest neighbor in the ab plane.

1. *Results: electronic properties-p6*

To understand the impact of the defective rocksalt structure on the electronic properties of CrO_x/BTO, DFT calculations have been performed using the structural information inferred from XPD and TEM. The unit cell used is composed of six O and four Cr atoms, as suggested in the literature[173]. Starting from the atomic positions of the perfect rocksalt structure and performing *ab-initio* atomic relaxations, we find a strong displacement of the oxygen atoms. The charged O atoms tend to move away from the Cr vacancies for electrostatic reasons. The final crystal configuration of the defective rocksalt is reported in Fig. 18. Differently from the perfect rocksalt structure, we observe CrO_6 octahedra with nonequivalent Cr-O bonds and bond angles different from 90° The nonequivalent Cr-O bonds in-plane are 1.948 Åand 1.953 Å, whereas the Cr-O distance out-of-plane is 2.054 Å . These values are comparable with the corundum Cr_2O_3 phase, where the Cr-O distances are 1.965 Å and 2.016 Å[174]. The in-plane Cr-O-Cr bond angles are 87.3°, 92.7°, and 93.0°,whereas the out-of-plane Cr-O-Cr bond angle is 93.8°. The in-plane Cr-Cr distances are 2.70 Å and 2.83 Å, whereas it is 2.92 Å for the out-of-plane distances. In the corundum Cr_2O_3 phase, the Cr-Cr distances are 2.65 Å and 2.89 Å, as well comparable to our optimized values in the defective structure.

If we consider the tetragonal space group *Immm*, it strongly differs from the corundum phase from the structural point of view. However, in both structure Cr is surrounded by six oxygens forming a CrO_6 octahedron with similar Cr-O distances. Therefore, the physical behavior of the Cr states related to the connectivity at the Fermi level is expected to be similar. Furthermore, in both cases, we have distorted octahedra with a crystal field splitting the d manifold into t_{2g} and the e_g states. The Cr defect reduces the connectivity of the Cr sublattice, which is in turn expected to decrease the Cr bandwidth, favoring the antiferromagnetic insulating states, as in other transition-metal compounds[175–177]. Indeed, the number of first neighbors in the Cr sublattice is 12 for the perfect rocksalt and becomes seven in the defective rocksalt. Due to the randomness of the Cr holes in the structure, we can assume that every Cr atom has seven first neighbors on average. The connectivity is one of the main differences between the tetragonal and corundum structure. Indeed, the number of first neighbors in the Cr sublattice is five for the corundum phase and seven for the tetragonal phase of the Cr_2O_3. The octahedra are corner shared in the tetragonal phase, whereas face-shared and edge-shared octahedra are present in the corundum phase. In Fig. 16(a), we show the density of states (DOS) for the defective rocksalt and the corundum phase using U = 0 and 6 eV. In both cases, the system shows an insulating behavior and the low-energy region is dominated by the 3d Cr electrons. The defective rocksalt phase has a smaller energy gap due to the reduced number of nearest neighbors in the Cr sublattice. As expected, there are three electrons on every Cr atom that occupy the t_{2g} majority spin states. With U = 0, the system presents a 0.8 eV energy gap for the defective rocksalt phase and a 1.0 eV energy gap for the corundum phase (see Fig. 16(a), top panel). As can be seen from Fig. 16(b), the oxygen states are mainly located between -7.5 and -2.5 eV from

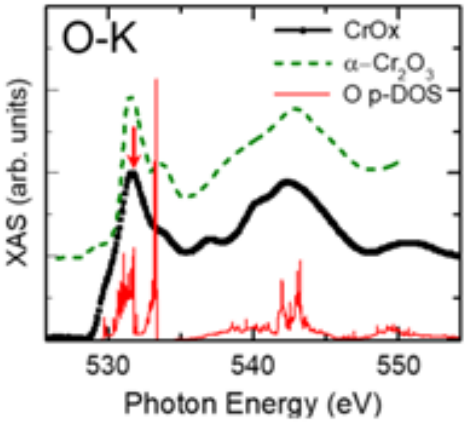

FIG. 17: XAS at the O K edge of Cr oxide on BTO (black curve) and reference α-Cr_2O_3 (green dashed curve)[179]. In red, the oxygen p-projected density of states (DOS) calculated from DFT on a defective rocksalt Cr_2O_3 structure is superimposed to match the experimental peaks.

the Fermi level. The occupied majority Cr electrons (Cr up in Fig. 16(b)) lie between -1.5 eV and the Fermi level, whereas the unoccupied majority electrons are located between 0.8 and 3.0 eV. The minority electrons (Cr down in Fig. 16(b)) are predominantly located between 1.5 and 4.5 eV. Upon increasing U, the size of the gap increases: for U = 0, 3, and 6 eV, the gap is 0.8, 2.1, and 3.2 eV, respectively, for the defective rocksalt. On the other hand, the bandwidth is barely affected. The band gap of the defective rocksalt is always lower than the gap of the corundum phase, which in the case of U = 6 eV is 3.7 eV.

As we can see from the bottom panel of Fig. 16(a), at U = 6 eV, the increase of the gap pushes the occupied d states towards the oxygen states, therefore increasing the hybridization between d and p states. In this case, the oxygen states are between -6.5 and -1.5 eV. The occupied majority Cr electrons lie mostly between -2.0 eV and the Fermi level, whereas the unoccupied majority electrons are between 3.2 and 5.0 eV. The minority electrons are mainly located between 4.0 and 7.0 eV.

The XAS spectra are very similar to those of corundum α-Cr_2O_3[178], indicating a strong analogy in the electronic structure of the two systems. This can be indeed related to the similar octahedral coordination of Cr with oxygen atoms, leading to similar crystal-field splitting of the d states. The O K XAS allows for a direct comparison between the calculated electronic structure and experimental data, since multiplet effects are not observed in the absorption spectra of ligands in transition metals[180]. From the DFT, we obtain that the first peak of the O K XAS indeed corresponds to the 3d contribution to the DOS, highlighted by an arrow on the first peak of Fig. 17. On the contrary, for the prediction of Cr-L XAS, a ligand field multiplet theory should be used so that we cannot directly compare it with the DFT-based DOS. We recall that following dipole selection rules, O 1s core electrons can be excited only to p states and it has been shown that a good correspondence can be found between the oxygen p states calculated within DFT and the oxygen K absorption spectra. Indeed, when the simulated oxygen p-projected DOS for Cr_2O_3 empty states is reported in Fig. 17, a clear correspondence between the O K XAS and the predicted empty states is found.

2. Results: magnetic properties of the defective Cr_2O_3-p7

To unveil the magnetic character of this compound, density functional theory calculations were performed on the structure determined in ref.[181] for tetragonal Cr_2O_3 grown on $BaTiO_3$ and reported in Fig. 18(a). According to our calculations, the magnetic moment of the Cr atoms in tetragonal Cr_2O_3 is 2.9 μ_B, very close to 3 μ_B that is the atomic limit of the spin moment of Cr^{3+}. We examined all the possible collinear spin configurations. The magnetic ground state is represented in Figure 1(a) We estimated the magnetic exchanges for the three inequivalent first-neighbors of the Cr sublattice. We described the Cr-Cr exchange interactions in terms of the classical Heisenberg Hamiltonian with spin S=1 where i and j run over the Cr-site. While the spin of the system is S=3/2, for simplicity the magnetic exchanges are reported for the spin S=1. The symbol <i,j> specifies that we take in account just the first-neighbors. In our convention both J_{ij} and J_{ji} must be considered. The system presents magnetic exchange along the a-axis (J_a), along the b-axis (J_b), and atoms with different z coordinate (J_c), as shown in Figure 1(b). We calculated the total energy of the three possible antiferromagnetic collinear phases with zero net magnetic moment since these magnetic phases are the closest to the ground state. From these energies we estimated the magnetic exchanges constants J_b

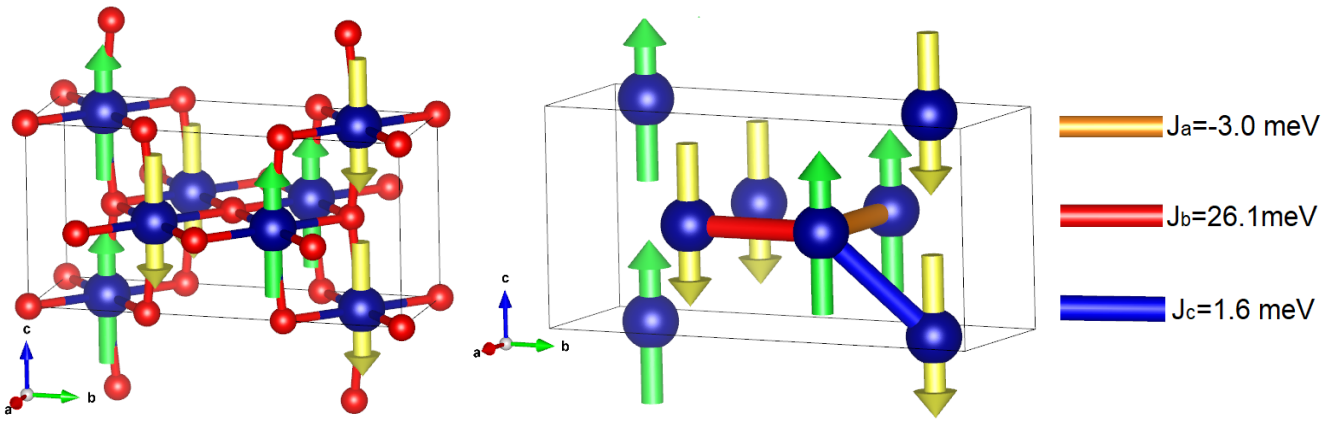

FIG. 18: Left panel: magnetic ground state from the DFT results fro U=6 eV. The up-spins (down-spins) are represented as green (yellow) arrows. The Cr and O atoms are represented as blue and red balls, respectively. Right panel: magnetic exchanges J_a , J_b and J_c with their numerical values. For a better visualization, the oxygen atoms are not shown.

and J_c. We doubled the cell along the a-axis and we repeat the procedure to obtain J_a.

We obtained a ferromagnetic exchange along the a-axis, whereas the magnetic exchanges along the J_b and J_c are antiferromagnetic. From a quantitative point of view, J_b=26.1 meV is the dominant magnetic exchange, while the other contributions result J_a=-3.0 meV and J_c=1.6 meV. Starting from the previous Heisenberg Hamiltonian in equation 3, it is possible to derive the critical temperature in the mean field approximation as $T_C^{MFA} = \frac{S(S+1)}{3}\frac{\sum_{i=1}^{n} J_{0,i}}{k_B}24$, where n is the number of first-neighbors and J_{0i} the magnetic exchange between the Cr atom and the i-th neighbor. Considering the connectivity from the Fig. 18(b), we have $T_C^{MFA}=\frac{2}{3}\frac{S+1}{2S}\frac{J_b+2J_a+4J_c}{k_B}$. Evaluating the previous formula using the numerical values of the magnetic exchange constants, the critical temperature in mean field approximation results 205 K for S=1 and 171 K for S=3/2.

Considering the experimental error bar, this measurement confirms the previous indications of antiferromagnetic character of tetragonal Cr_2O_3 with a transition at about 40 K. We note that this value is significantly smaller than that of bulk α-Cr_2O_3 (311 K). The transition temperature predicted by *ab-initio* calculations for the tetragonal phase (205 K) is already smaller than the one of the corundum phase just because the different structure determines a lower magnetic coupling between Cr atoms of the two structures. Moreover, this theoretical critical temperature calculated in mean field approximation is generally overestimated. As a matter of fact, this method works quite well in the case of high-dimensions and large connectivity. When the magnetic sublattice presents low connectivity as the Cr sublattice in tetragonal Cr_2O_3, instead, the experimental critical temperature can be lower, as already demonstrated in other low-connectivity oxides[183,184]. Additionally, defects and inhomogeneity, which are related to weak localization experimentally observed through noise spectroscopy, can lower the critical transition temperature from the ideal case considered in theoretical calculations. Finally, a reduction of the transition temperature in thin films has been observed for α-Cr_2O_3, films when thickness is comparable with the spin correlation length.[185] A similar finite-size scaling effect could also be present in our ultrathin films of tetragonal Cr_2O_3.

B. Summary for the tetragonal chromium (III) oxide

We discuss the chemical and structural properties of Cr thin films grown on a $BaTiO_3$ template. We observed a progressive oxidation of the chromium layer, which we related to the thermally activated migration of oxygen from the substrate. From experimental and theoretical investigations, a +3 chromium oxidation state was found. XPD, electron diffractions, and TEM showed a defective rocksalt structure, with one out of every three atoms of chromium missing in order to preserve the stoichiometry (Cr_2O_3). The structure grows lattice matched on the underlying $BaTiO_3$ layer. Despite the structural difference with respect to the corundum α-Cr_2O_3 phase, we demonstrated both experimentally (XAS) and theoretically (DFT) that the electronic properties are basically equivalent. This can be ascribed to the similar octahedral coordination of oxygen atoms, leading to similar crystal-field splitting of the d-states in the two configurations.

We discussed the magnetic properties of this tetragonal phase of Cr_2O_3, and the interfacial effects between this magnetic oxide and a neighboring Pt layer. The DFT results show that the tetragonal Cr_2O_3 con be considered as a correlated compound with low connectivity and predicts an antiferromagnetic ground state. From electrical measurements, we show that sizeable magnetotransport effects both in longitudinal and transverse measurement

configurations can be observed at this interface, both pointing out a magnetic phase transition at about 40 K.

VII. FINAL SUMMARY

Our study highlights TMO in the low connectivity limit as a platform for engineering the interplay among electronic, structural and magnetic properties. It may represent a useful basis to explore the relevant mechanisms that determine the collective quantum behavior as well as the response upon an external perturbation, to produce new exotic phases and new features in electronic transport in complex oxide heterostructures opening new possibilities to manipulate the electronic, orbital and spin degrees of freedom by a selective choice and tailoring of their interfaces and surfaces. This approach of tuning heterointerfaces and surfaces by coupling structural, electronic and magnetic properties can be extended to other material systems with promising prospects for future oxide electronic and spintronic devices.

[1] H. Y. Hwang, Y. Iwasa, M. Kawasaki, B. Keimer, N. Nagaosa, and Y. Tokura, Nature Mat. **11**, 103 (2012).
[2] Interface Physics in Complex Oxide Heterostructures, Pavlo Zubko, Stefano Gariglio, Marc Gabay, Philippe Ghosez, Jean-Marc Triscone, Annual Review of Condensed Matter Physics 2:1, 141-165 (2011).
[3] Magnetism manipulation in ferromagnetic/ferroelectric heterostructures by electric field induced strain, Xiaobin Guo, Dong Li and Li Xi, Chinese Physics B, Volume 27, Number 9 (2018).
[4] Interface-induced phenomena in magnetism, Frances Hellman et al., Rev. Mod. Phys. 89, 025006 (2017).
[5] Interface Characterization and Control of 2D Materials and Heterostructures, Xiaolong Liu Mark C. Hersam, Adv. Mater. 30, 1801586 (2018).
[6] M. Imada, A. Fujimori, and Y. Tokura, Rev. Mod. Phys. **70**, 1039 (1998).
[7] J. Heber, Nature **459**, 28-30 (2009).
[8] A. Ohtomo, D. A. Muller, J. L. Grazul, and H. Y. Hwang, Nature **419**, 378-80 (2002).
[9] A. Gozar, Nature **455**, 782-5 (2008).
[10] A. Ohtomo and H. Y. Hwang, Nature **427**, 423-6 (2004).
[11] N. Nakagawa, H. Y. Hwang, and D. A. Muller, Nature Mater. **5**, 204-9 (2006).
[12] Y. Tokura and H. Y. Hwang, Nature Mater. **7**, 694-5 (2008).
[13] E. Dagotto, Science **318**, 1076 (2007).
[14] Y. Maeno, H. Hashimoto, K. Yoshida, S. Nishizaki, T. Fujita, J. G. Bednorz, and F. Lichtenberg, Nature **372**, 532 (1994).
[15] S. Ikeda, Y. Maeno, S. Nakatsuji, M. Kosaka, and Y. Uwatoko, Phys. Rev. B **62**, R6089 (2000).
[16] R. S. Perry, L. M. Galvin, S. A. Grigera, L. Capogna, A. J. Schofield, A. P. Mackenzie, M. Chiao, S. R. Julian, S. I. Ikeda, S. Nakatsuji, Y. Maeno, Phys. Rev. Lett. **86**, 2661 (2001).
[17] S. A. Grigera, R. S. Perry, A. J. Schofield, M. Chiao, S. R. Julian, G. G. Lonzarich, S. I. Ikeda, Y. Maeno, A. J. Millis, and A. P. Mackenzie, Science **294**, 329 (2001).
[18] G. Cao, L. Balicas, W. H. Song, Y. P. Sun, Y. Xin, V. A. Bondarenko, J. W. Brill, S. Parkin, and X. N. Lin, Phys. Rev. B **68**, 174409 (2003).
[19] Z. Q. Mao, M. Zhou, J. Hooper, V. Golub, and C. J. O'Connor, Phys. Rev. Lett. **96**, 077205 (2006).
[20] R. Gupta, M. Kim, H. Barath, S. L. Cooper, and G. Cao, Phys. Rev. Lett. **96**, 067004 (2006).
[21] P. B. Allen, H. Berger, O. Chauvet, L. Forro, T. Jarlborg, A. Junod, B. Revaz, and G. Santi, Phys. Rev. B **53**, 4393 (1996).
[22] G. Kresse and J. Furthmüller, Comput. Mat. Sci. **6**, 15 (1996).
[23] G. Kresse and D. Joubert, Phys. Rev. B **59**, 1758 (1999).
[24] P. E. Blöchl, Projector augmented-wave method, Phys. Rev. B **50**, 17953 (1994).
[25] J. P. Perdew, K. Burke, and M. Ernzerhof, Phys. Rev. Lett. **77**, 3865 (1996).
[26] J. P. Perdew, A. Ruzsinszky, G. I. Csonka, O. A. Vydrov, G. E. Scuseria, L. A. Constantin, X. Zhou, and K. Burke Restoring the density-gradient expansion for exchange in solids and surfaces, Phys. Rev. Lett. 100, 136406 (2008).
[27] V. I. Anisimov, J. Zaanen, and O. K. Andersen, Band theory and Mott insulators: Hubbard U instead of Stoner I , Phys. Rev. B 44, 943 (1991).
[28] A. I. Liechtenstein, V. I. Anisimov, and J. Zaanen, Densityfunctional theory and strong interactions: Orbital ordering in Mott-Hubbard insulators, Phys. Rev. B 52, 5467(R) (1995).
[29] V. I. Anisimov, F. Aryasetiawan and A. I. Lichtenstein, J. Phys.: Condens. Matter **9** (1997) 767-808.
[30] L. Vaugier, H. Jiang, and S. Biermann Phys. Rev. B 86, 165105 (2012).
[31] J. C. Slater and G. F. Koster, Phys. Rev. **94**, 1498-1524 (1954).
[32] N. Marzari and D. Vanderbilt, Phys. Rev. B **56**, 12847 (1997).
[33] I. Souza, N. Marzari, and D. Vanderbilt, Phys. Rev. B **65**, 035109 (2001).
[34] A. A. Mostofi, J. R. Yates, Y. S. Lee, I. Souza, D. Vanderbilt, and N. Marzari, Comput. Phys. Comm. **178**, 685 (2008).
[35] G. Cuono, C. Autieri, F. Forte, M. T. Mercaldo, A. Romano, A. Avella, and C. Noce, New J. Phys. **21**, 063027 (2019).

[36] G. Cuono, F. Forte, M. Cuoco, R. Islam, J. Luo, C. Noce, and C. Autieri, Phys. Rev. Mater. **3**, 095004 (2019).
[37] K. Yoshimatsu, T. Okabe, H. Kumigashira, S. Okamoto, S. Aizaki, A. Fujimori, and M. Oshima, Phys. Rev. Lett. 104, 147601 (2010).
[38] P. Zubko, S. Gariglio, M. Gabay, P. Ghosez, and J.-M. Triscone, Annu. Rev. Condens. Matter Phys. 2, 141 (2011).
[39] J. Hubbard, Proc. R. Soc. A 276, 238 (1963).
[40] A. V. Boris, Y. Matiks, E. Benckiser, A. Frano, P. Popovich, V. Hinkov, P.Wochner, M. Castro-Colin, E. Detemple, V. K. Malik, C. Bernhard, T. Prokscha, A. Suter, Z. Salman, E. Morenzoni, G. Cristiani, H.-U. Habermeier, and B. Keimer, Science 332, 937 (2011).
[41] P. D. C. King, H. I.Wei, Y. F. Nie, M. Uchida, C. Adamo, S. Zhu, X. He, I. Božović, D. G. Schlom, and K. M. Shen, Nat. Nanotechnol. 9, 443 (2014).
[42] R. Scherwitzl, S. Gariglio, M. Gabay, P. Zubko, M. Gibert, and J.-M. Triscone, Phys. Rev. Lett. 106, 246403 (2011).
[43] S. Jana, S. G.Bhat, B. C. Behera, L. Patra, P. S. Anil Kumar, B. R. K. Nanda, D. Samal, Localization Crossover Near Metal-Insulator Transition in Two-Dimension Limit of $CaCu_3Ru_4O_{12}$, arXiv:1908.11128 (2019).
[44] Seung Gyo Jeong, Taewon Min, Sungmin Woo, Jiwoong Kim, Yu-Qiao Zhang, Seong Won Cho, Jaeseok Son, Young-Min Kim , Jung Hoon Han, Sungkyun Park, Hu Young Jeong, Hiromichi Ohta, Suyoun Lee, Tae Won Noh, Jaekwang Lee, and Woo Seok Choi Phys. Rev. Lett. **124**, 026401 (2020).
[45] D. Toyota *et al.*, Appl. Phys. Lett. **87** 162508 (2005).
[46] J. Xia *et al.*, Phys. Rev. B. **79** 140407(R) (2009).
[47] Y. J. Chang *et al.*, Phys. Rev. Lett. **103**, 057201 (2009).
[48] C. S. Alexander *et al.*, Phys. Rev. B **60**, R8422 (1999).
[49] E. Gorelov, M. Karolak, T. O. Wehling, F. Lechermann, A. I. Lichtenstein, and E. Pavarini, Phys. Rev. Lett. **104**, 226401 (2010).
[50] X. Ke *et al.*, Phys. Rev. B **84**, 201102 (2011).
[51] J. H. Jung *et al.*, Phys. Rev. Lett. **91**, 056403 (2003).
[52] H.-T. Jeng *et al.*, Phys. Rev. Lett. **97**, 067002 (2006).
[53] K. Gupta, B. Mandal and P. Mahadevan, Phys. Rev. B **90**, 125109 (2014).
[54] G. Rijnders *et al.*, Appl. Phys. Lett. **84**, 505 (2004).
[55] R. Matzdorf, Z. Fang, Ismail, Jiandi Zhang, T. Kimura, Y. Tokura, K. Terakura, and E. W. Plummer, Science **289**, 746 (2000).
[56] Etz C. *et al.* Phys. Rev. B. **86**, 064441 (2012).
[57] A. T. Zayak *et al.*, Phys. Rev. B **74**, 094104 (2006).
[58] M. Shishkin, T. Ziegler, Surf. Sci. **606**, 1078-1087 (2012).
[59] Z.-Q. Li *et al.*, Phys. Rev. B **58**, 8075 (1998). M.-Q. Cai *et al.*, J. Chem. Phys **124**, 174701 (2006).
[60] C. Autieri, M. Cuoco and C. Noce, Phys. Rev. B **89**, 075102 (2014).
[61] K. Maiti, Phys. Rev. B **73**, 235110 (2006).
[62] A. T. Zayak *et al.*, Phys. Rev. B **77**, 214410 (2008).
[63] J. M. Rondinelli *et al.*, Phys. Rev. B **78**, 155107 (2008).
[64] M. Verissimo-Alves *et al.*, Phys. Rev. Lett. **108**, 107003 (2012).
[65] M. Gu, Q. Xie, X. Shen, R. Xie, J. Wang, G. Tang, D. Wu, G. P. Zhang, and X. S. Wu, Phys. Rev. Lett. **109**, 157003 (2012).
[66] C. W. Jones *et al.*, Acta Crystallogr., Sect. C: Cryst. Struct. Commun. **45**, 365 (1989).
[67] O. Friedt. *et al*, Phys. Rev. B **63**, 174432 (2000).
[68] B. Hu, G. T. McCandless, M. Menard, V. B. Nascimento, J. Y. Chan, E. W. Plummer, and R. Jin, Phys. Rev. B **81**, 184104 (2010).
[69] C. Autieri, J. Phys.: Condens. Matter **28**, 42 (2016).
[70] C. Cirillo, V. Granata, G. Avallone, R. Fittipaldi, C. Attanasio, A. Avella, and A. Vecchione, Phys. Rev. B **100**, 235142 (2019).
[71] B. J. Kim, H. Jin, S. J. Moon, J.-Y. Kim, B.-G. Park, C. S. Leem, J. Yu, T.W. Noh, C. Kim, S.-J. Oh et al., Phys. Rev. Lett. 101, 076402 (2008).
[72] B. J. Kim, H. Ohsumi, T. Komesu, S. Sakai, T. Morita, H. Takagi, and T. Arima, Science 323, 1329 (2009).
[73] J. K. Kawasaki, M. Uchida, H. Paik, D. G. Schlom, and K. M. Shen, Phys. Rev. B 94, 121104 (2016).
[74] Y. F. Nie, P. D. C. King, C. H. Kim, M. Uchida, H. I. Wei, B. D. Faeth, J. P. Ruf, J. P. C. Ruff, L. Xie, X. Pan et al., Phys. Rev. Lett. 114, 016401 (2015).
[75] I. Pallecchi, M. T. Buscaglia, V. Buscaglia, E. Gilioli, G. Lamura, F. Telesio, M. R. Cimberle, and D. MarrÂťe, J. Phys. Condens. Matter 28, 065601 (2016).
[76] K.-H. Kim, H.-S. Kim, and M. J. Han, J. Phys. Condens. Matter 26, 185501 (2014).
[77] J. Matsuno, K. Ihara, S. Yamamura, H. Wadati, K. Ishii, V. V. Shankar, H.-Y. Kee, and H. Takagi, Phys. Rev. Lett. 114, 247209 (2015).
[78] S. Y. Kim, C. H. Kim, L. J. Sandilands, C. H. Sohn, J. Matsuno, H. Takagi, K.W. Kim, Y. S. Lee, S. J. Moon, and T.W. Noh, Phys. Rev. B 94, 245113 (2016).
[79] L. Hao, D. Meyers, C. Frederick, G. Fabbris, J. Yang, N. Traynor, L. Horak, D. Kriegner, Y. Choi, J.-W. Kim, D. Haskel, P. J. Ryan, M. P. M. Dean, and J. Liu, Phys. Rev. Lett. 119, 027204 (2017).
[80] D. Meyers, Y. Cao, G. Fabbris, N. J. Robinson, L. Hao, C. Frederick, N. Traynor, J. Yang, J. Lin, M. Upton et al., Scientific Reports **9**, Article number: 4263 (2019).

[81] B. Kim, P. Liu, and C. Franceschini (to be published).
[82] P. Schütz, D. D. Sante, L. Dudy, J. Gabel, M. Stübinger, M. Kamp, Y. Huang, M. Capone, M.-A. Husanu, V. Strocov, G. Sangiovanni, M. Sing, and R. Claessen, following Letter, Phys. Rev. Lett. 119, 256404 (2017).
[83] H.-S. Kim, Y. Chen, and H.-Y. Kee, Phys. Rev. B 91, 235103 (2015).
[84] M. A. Zeb and H.-Y. Kee, Phys. Rev. B 86, 085149 (2012).
[85] H. Watanabe, T. Shirakawa, and S. Yunoki, Phys. Rev. B 89, 165115 (2014).
[86] C. Autieri, J. Phys. Condens. Matter 28, 426004 (2016).
[87] J. Hwang, J. Son, J. Y. Zhang, A. Janotti, C. G. Van deWalle, and S. Stemmer, Phys. Rev. B 87, 060101 (2013).
[88] R. Fittipaldi, A. Vecchione, S. Fusanobori, K. Takizawa, H. Yaguchi, J. Hooper, R. S. Perry, and Y. Maeno, J. Cryst. Growth **282**, 152 (2005).
[89] R. Ciancio, H. Petterson, J. Börjesson, S. Lopatin, R. Fittipaldi, A. Vecchione, S. Kittaka, Y. Maeno, S. Pace, and E. Olsson, Appl. Phys. Lett. **95**, 142507 (2009).
[90] R. Fittipaldi, D. Sisti, A. Vecchione, S. Pace, Cryst. Growth and Design, **7**, 2495 (2007).
[91] T. Shiroka, R. Fittipaldi, M. Cuoco, R. De Renzi, Y. Maeno, R. J. Lycett, S. Ramos, E. M. Forgan, C. Baines, A. Rost, V. Granata and A. Vecchione, Phys. Rev. B **85**, 134527 (2012).
[92] J. Hooper, M. Zhou, Z. Q. Mao, Y. Liu, R. S. Perry, and Y. Maeno, Phys. Rev. B **73**, 132510 (2006).
[93] R. Fittipaldi, A. Vecchione, R. Ciancio, S. Pace, M. Cuoco, D. Stornaiuolo, D. Born, F. Tafuri, E. Olsson, S. Kittaka, H. Yaguchi, and Y. Maeno, Europhys. Lett. **83**, 27007 (2008).
[94] M. A. Zurbuchen, Y. Jia, S. Knapp, A. H. Carim, D. G. Schlom, L. Zou, and Y. Liu, Appl. Phys. Lett. **78**, 2351 (2001); M. A. Zurbuchen, Y. Jia, S. Knapp, A. H. Carim, D. G. Schlom, and X. Q. Pan, Appl. Phys. Lett. **83**, 3891 (2003).
[95] W. Tian, J. H. Haeni, D. G. Schlom, E. Hutchinson, B. L. Sheu, M. M. Rosario, P. Schiffer, Y. Liu, M. A. Zurbuchen, and X. Q. Pan, Appl. Phys. Lett. **90**, 022507 (2007).
[96] Y. Krockenberger *et al.*, Appl. Phys. Lett. **97**, 082502 (2010).
[97] P. Hohenberg and W. Kohn, Phys. Rev. **136**, B864 (1964), W. Kohn and L. J. Sham, Phys. Rev. **140**, 1133 (1964).
[98] X. Gonze, G. M. Rignanese, M. Verstraete, J. M. Beuken, Y. Pouillon, R. Caracas, F. Jollet, M. Torrent, G. Zerah, M. Mikami, P. Ghosez, M. Veithen, J. Y. Raty, V. Olevano, F. Bruneval, L. Reining, R. Godby, G. Onida, D. R. Hamann, and D. C. Allan, Zeit. Kristallogr. **220**, 558 (2005).
[99] Z. Wu and R. E. Cohen, Phys. Rev. B **73**, 235116 (2006).
[100] M. Fuchs, M. Scheffler, Comput. Phys. Commun. **119**, 67 (1999).
[101] D. I. Bilc and Ph. Ghosez *et al.*, Phys. Rev. B **77**, 165107 (2008).
[102] M. W. Haverkort, I. S. Elfimov, L. H. Tjeng, G. A. Sawatzky, and A. Damascelli, Phys. Rev. Lett. **101**, 026406 (2008).
[103] J. Mravlje, M. Aichhorn, T. Miyake, K. Haule, G. Kotliar, and A. Georges, Phys. Rev. Lett. **106**, 096401 (2011).
[104] C. N. Veenstra, Z.-H. Zhu, B. Ludbrook, M. Capsoni, G. Levy, A. Nicolaou, J. A. Rosen, R. Comin, S. Kittaka, Y. Maeno, I. S. Elfimov, and A. Damascelli, Phys. Rev. Lett. **110**, 097004 (2013).
[105] T. Oguchi, Phys. Rev. B **51**, 1385 (1995).
[106] D. J. Singh, Phys. Rev. B **52**, 1358 (1995).
[107] A. Liebsch and A. Lichtenstein, Phys. Rev. Lett. **84**, 1599 (2000).
[108] O. Chmaissen, J. D. Jorgensen, H. Shaked, S. Ikeda, and Y. Maeno, Phys. Rev. B **57**, 5067 (1998).
[109] A. Tamai, M. P. Allan, J. F. Mercure, W. Meevasana, R. Dunkel, D. H. Lu, R. S. Perry, A. P. Mackenzie, D. J. Singh, Z. X. Shen, and F. Baumberger, Phys. Rev. Lett. **101**, 026407 (2008).
[110] A. V. Puchkov, Z.-X. Shen, and G. Cao, Phys. Rev. B **58**, 6671 (1998).
[111] D. J. Singh and I. I. Mazin Phys. Rev. B **63**,165101 (2001).
[112] Q. Huang J. W. Lynn and R. W. Erwin J. Jarupatrakorn and R. J. Cava Phys. Rev. B **58**, 8515 (1998).
[113] C. Piefke and F. Lechermann Phys. Status Solidi B **248**, 2269 (2011).
[114] X. Gonze, B. Amadon, P. M. Anglade, J. M. Beuken, F. Bottin, P. Boulanger, F. Bruneval, D. Caliste, R. Caracas, M. Cote, T. Deutsch, L. Genovese, P. Ghosez, M. Giantomassi, S. Goedecker, D. R. Hamann, P. Hermet, F. Jollet, G. Jomard, S. Leroux, M. Mancini, S. Mazevet, M. J. T. Oliveira, G. Onida, Y. Pouillon, T. Rangel, G. M. Rignanese, D. Sangalli, R. Shaltaf, M. Torrent, M. J. Verstraete, G. Zerah, J. W. Zwanziger, Computer Phys. Comm. **180**, 2582 (2009).
[115] Y. Yanase, J. Phys. Soc. Jpn. **82**, 044711 (2013).
[116] C. Autieri, M. Cuoco, and C. Noce, Phys. Rev. B **85**, 075126 (2012).
[117] M. Gibert, P. Zubko, R. Scherwitzl, J. Íñiguez and J-M Triscone, Nat. Mater. **11**, 195, (2012).
[118] F. Bern, M. Ziese, I. Vrejoiu, X. Li and P. A. van Aken, New J. Phys. **18**, 053201 (2016).
[119] U. Lüders *et al.*, Phys. Rev. B **80**, 241102 R (2009).
[120] B. R. K. Nanda, S. Satpathy, and M. S. Springborg, Phys. Rev. Lett. **98**, 216804 (2007).
[121] H. Boschker *et al.*, Phys. Rev. Lett. **109**, 157207 (2012).
[122] A. Paul, C. Reitinger, C. Autieri, B. Sanyal, W. Kreuzpaintner, J. Jutimoosikm, R. Yimnirun, F. Bern, P. Esquinzi, P. Korelis and P. Böni, Appl. Phys. Lett. **105**, 022409 (2014).
[123] S. Roy, C. Autieri, B. Sanyal and T. Banerjee. Sci. Rep. **5**, 15747 (2015).
[124] S. R. Lee, M. S. Anwar, Y. J. Shin, M.-C. Lee, Y. Sugimoto, M. Kunieda, S. Yonezawa, Y. Maeno, T. W. Noh. Preprint available at https://arxiv.org/abs/1609.03010.
[125] C. Autieri, O. Maistrenko, C. Noce, A. Romano, D. Manske, P. Gentile and M. Cuoco. In manuscript.
[126] G. Koster *et al.*, Rev. Mod. Phys. **84**, 253 (2012).
[127] Parui S., Klandermans P. S., Venkatesan S., Scheu C. & Banerjee T. *J. Phys.: Condens. Matter* **25**, 445005 (2013).
[128] Kaiser W. J. & Bell L. D. *Phys. Rev. Lett.* **60**, 1406 (1988).

[129] Rana K. G., Yajima T., Parui S., Kemper A. F., Devereaux T. P., Hikita Y., Hwang H. Y. & Banerjee T. *Sci. Rep.* **3**, 1274 (2013).
[130] Roy S., Kamerbeek A. M., Rana K. G., Parui S. & Banerjee T. *Appl. Phys. Lett.* **102**, 192909 (2013).
[131] Banerjee T., Lodder J. C. & Jansen R. *Phys. Rev. B* **76**, 140407(R) (2007).
[132] Prietsch M. *Phys. Rep.* **253**, 163 (1995).
[133] J. Nogués and I. K. Schuller, J. Magn. Magn. Mater. **192** 203 (1999).
[134] K. Ueda, H. Tabata and T. Kawai, Science **280** 1064, (1998).
[135] H. Wadati, J. Okamoto, M. Garganourakis, V. Scagnoli, U. Staub, Y. Yamasaki, H. Nakao, Y. Murakami, M. Mochizuki, M. Nakamura, M. Kawasaki, and Y. Tokura, Phys. Rev. Lett. **108**, 047203 (2012).
[136] D. Okuyama, S. Ishiwata, Y. Takahashi, K. Yamauchi, S. Picozzi, K. Sugimoto, H. Sakai, M. Takata, R. Shimano, Y. Taguchi, T. Arima, and Y. Tokura, Phys. Rev. B **84**, 054440 (2011).
[137] F. Jiménez-Villacorta, J. A. Gallastegui, I. Fina, X. Marti, and J. Fontcuberta, Phys. Rev. B **86**, 024420 (2012).
[138] C. He A. J. Grutter, M. Gu, M. D. Browning, Y. Yakamura, B. J. Kirby, J. A. Borchers, J. W. Kim, M. R. Fitzsimmons, X. Zhai, V. V. Mehta, F. J. Wong, and Y. Sizuki, Phys. Rev. Lett. **109**, 197202 (2012).
[139] J.-I. Hong, T. Leo, D. J. Smith and A. E. Berkowitz, Phys. Rev. Lett. **96**, 117204 (2006).
[140] H. Ohldag, A. Scholl, F. Nolting, E. Arenholz, S. Maat, A. T. Young, M. Carey, J. Stöhr, Phys. Rev. Lett. **91**, 017203 (2003); H. Ohldag, H. Shi, E. Arenholz, J. Stöhr and D. Lederman, Phys. Rev. Lett. **96**, 027203 (2006).
[141] M. Gruyters and D. Schmitz, Phys. Rev. Lett. **100**, 077205 (2008).
[142] U. Nowak, K. D. Usadel, J. Keller, P. Miltényi, B. Beschoten, and G. Güntherodt, Phys. Rev. B **66**, 014430 (2002).
[143] C. Zandalazini, P. Esquinazi, G. Bridoux, J. Barzola-Quiquia, H. Ohldag and E. Arenholz, J. Magn. Magn. Mater. **323**, 2892 (2011).
[144] A. Paul, C. Zandalazini, P. Esquinazi, C. Autieri, B. Sanyal, P. Korelis and P. Böni, J. Appl. Crystallogr. **47**, 1054 (2014).
[145] E. C. Passamania, C. Laricaa, C. Marquesa, J. R. Provetia, A. Y. Takeuchib and F. H. Sanchez, J. Magn. Magn. Mater. **299**, 11 (2006).
[146] R. K. Zheng, G. H. Wen, K. K. Fung, and X. X. Zhang, J. Appl. Phys. **95**, 5244 (2004).
[147] J. de la Venta, M. Erekhinsky, Siming Wang, K. G. West, R. Morales, and Ivan K. Schuller, Phys. Rev. B **85**, 134447 (2012).
[148] S. J. Yuan *et al.*, Phys. Rev. B **88**, 024413 (2013).
[149] C. Autieri and B. Sanyal, New J. Phys. **16**, 113031 (2014).
[150] C. Ma, Z. Yang and S. Picozzi J. Phys.: Condens. Matter **18**, 7717 (2006).
[151] G. Colizzi, A. Filippetti, and V. Fiorentini, Phys. Rev. B **76**, 064428 (2006).
[152] A. Hoffmann *et al.*, Phys. Rev. B **66**, 220406(R) (2002).
[153] S. Picozzi, K. Yamauchi, G. Bihlmayer and S. Blügel, Phys. Rev. B **74**, 094402 (2006).
[154] K. Yamauchi, F. Freimuth, S. Blügel, and S. Picozzi, Phys. Rev. B **78**, 014403 (2008).
[155] *Landolt-Börnstein*, Vol. III/19a, ed. by H.P.J. Wijn (Springer Berlin 1986).; Cullity, B. D.; Graham, C.D. (2005). Introduction to Magnetic Materials.; Phys. Rev. B **41**, 11919 (1990).
[156] Y. Suzuki *et al.*, J. Appl. Phys. **83**, 7064 (1998).
[157] W. H. Meiklejohn and C. P. Bean, Phys. Rev. **102**, 1413 (1956).
[158] C.-G. Duan *et al.*, Phys. Rev. Lett. **97**, 047201 (2006).
[159] L. Bocher *et al.*, NanoLett. 2012, **12**, 376-382.
[160] S. Valencia *et al.*, Nat. Mater. **10**, 753 (2011).
[161] G.Radaelli et al., Electric control of magnetism at the Fe/$BaTiO_3$ interface, Nat. Commun. 5, 3404 (2014).
[162] A. Paul et al., Exotic exchange bias at epitaxial ferroelectric ferromagnetic interfaces, Appl. Phys. Lett. 105, 022409 (2014).
[163] S. Hausmann et al., Atomic-scale engineering of ferroelectric ferromagnetic interfaces of epitaxial perovskite films for functional properties, Sci. Rep. 7, 10734 (2017).
[164] C.-G. Duan, S. S. Jaswal, and E. Y. Tsymbal, Predicted Magnetoelectric Effect in Fe/$BaTiO_3$ Multilayers: Ferroelectric-Control of Magnetism, Phys. Rev. Lett. 97, 047201 (2006).
[165] M. Asa, L. Baldrati, C. Rinaldi, S. Bertoli, G. Radaelli, M. Cantoni, and R. Bertacco, Electric field control of magnetic properties and electron transport in $BaTiO_3$-based multiferroic heterostructures, J. Phys.: Condens. Matter 27, 504004 (2015).
[166] W. Eerenstein, M. Wiora, J. L. Prieto, J. F. Scott and N. D. Matur, Giant sharp and persistent converse magnetoelectric effects in multiferroic epitaxial heterostructures, Nat. Mater. 6, 348 (2007).
[167] G. Radaelli, D. Gutiérrez, F. Sanchéz, R. Bertacco, M. Stengel, and J. Fontcuberta, Large room-temperature electroresistance in dual-modulated ferroelectric tunnel barriers, Adv. Mater. 27, 2602 (2015).
[168] D. J. Kim, H. Lu, S. Ryu, C.-W. Bark, C.-B. Eom, E.Y. Tsymbal, and A. Gruverman, Ferroelectric tunnel memristor, Nano Lett. 12, 5697 (2012).
[169] A. K. Bainand, P. Chand ,Ferroelectrics (Wiley-VCH, NewYork, 2017).
[170] G. B. Haxel, J. B. Hedrick, and G. J. Orris, Rare Earth Elements-Critical Resources for High Technology, U.S. Geological Survey, 087-02 (2005), http://pubs.usgs.gov/fs/ 2002/fs087-02.
[171] C. Autieri and C. Noce, Philos. Mag. 97, 3276 (2017).
[172] A. Jain, S. P. Ong, G. Hautier, W. Chen, W. D. Richards, S. Dacek, S. Cholia, D. Gunter, D. Skinner, G. Ceder, and K. A. Persson, APL Mater. 1, 11002 (2013).
[173] X. S. Du, S. Hak, T. Hibma, O. C. Rogojanu, and B. Struth, X-rays diffraction on a new chromium oxide single-crystal thin film prepared by molecular beam epitaxy, J. Cryst. Growth 293, 228 (2006).

[174] G. K. Lewis and H. G. Drickamer, Effect of high pressure on the lattice parameters of Cr_2O_3 and α-Fe2O3, J. Chem. Phys. 45, 224 (1966).
[175] C. Autieri, Antiferromagnetic and xy ferro-orbital order in insulating $SrRuO_3$ thin films with SrO termination, J. Phys. Condens. Matter 28, 426004 (2016).
[176] S. A. Ivanov et al., Polar order and frustrated antiferromagnetism in perovskite Pb2MnWO6 single crystals, Inorg. Chem. 55, 2791 (2016).
[177] D. J. Groenendijk et al., Spin-Orbit Semimetal $SrIrO_3$ in the Two-Dimensional Limit, Phys. Rev. Lett. 119, 256403 (2017).
[178] M. Asa, G. Vinai, J. L. Hart, C. Autieri, C. Rinaldi, P. Torelli, G. Panaccione, M. L. Taheri, S. Picozzi and M. Cantoni: Interdiffusion-driven synthesis of cubic Chromium (III) oxide on $BaTiO_3$. Phys. Rev. Materials **2**, 033401 (2018).
[179] F. M. F. De Groot, M. Grioni, J. C. Fuggle, J. Ghijsen, G. A. Sawatzky, and H. Petersen, Oxygen 1s x-ray-absorption edges of transition-metal oxides, Phys. Rev. B **40**, 5715 (1989).
[180] F. de Groot and A. Kotani, Core Level Spectroscopy of Solids (CRC Press, Boca Raton, 2008)
[181] M. Asa, G. Vinai, J. L. Hart, C. Autieri, C. Rinaldi, P. Torelli, G. Panaccione, M. L. Taheri, S. Picozzi, and M. Cantoni, Phys. Rev. Mater. 2, 033401 (2018).
[182] E. Şaşioğlu, L. M. Sandratskii, and P. Bruno, Phys. Rev. B 70, 24427 (2004).
[183] S. A. Ivanov, A. A. Bush, A. I. Stash, K. E. Kamentsev, V. Y. Shkuratov, Y. O. Kvashnin, C. Autieri, I. Di Marco, B. Sanyal, O. Eriksson, P. Nordblad, and R. Mathieu, Inorg. Chem. 55, 2791 (2016).
[184] X. Ming, C. Autieri, K. Yamauchi, and S. Picozzi, Phys. Rev. B 96, 205158 (2017).
[185] S. P. Pati, M. Al-Mahdawi, S. Ye, Y. Shiokawa, T. Nozaki, and M. Sahashi, Phys. Rev. B 94, 224417 (2016).

5. Informacja o wykazywaniu się istotną aktywnością naukową albo artystyczną realizowaną w wiÂęcej niż jednej uczelni, instytucji naukowej lub instytucji kultury, w szczególności zagranicznej.

6. Informacja o osiągnięciach dydaktycznych, organizacyjnych oraz popularyzujących naukę lub sztukę.
Po uzyskaniu stopnia doktora:
a) Tutorial about applications of Density Functional Theory in the Biplab Sanyal lecture at the Summer School: "Magnetic solotronics in semiconductors and Dirac materials" in Como (Italy), 15-20 June 2015.
b) Course for candidate Ph.D. students at the Università degli Studi di Salerno. Title of the course: Density Functional Theory and beyond, concepts and applications, April 2017.
c) Lecture about "Introduction to the DFT" at the Master students of Università degli Studi di Salerno, April 2017.
d) Course for candidate Ph.D. students at the Università degli Studi di Salerno. Title of the course: Magnetism and electronic correlations in density functional theory, May 2018.

7. Oprócz kwestii wymienionych w pkt. 1-6, wnioskodawca może podać inne informacje, ważne z jego punktu widzenia, dotyczące jego kariery zawodowej/ In addition to the issues listed in point 1-6, the applicant may provide other information, important from his point of view, regarding his professional career.

I performed all the theoretical calculations for the all papers p1-p7 presented, the band structure calculation for the publication p5. S. Roy author of p3 and A. M. R. V. L. Monteiro author of p5 were experimental Ph.D. students that quitted science and they did not reply to me. Prof. T. Banerjee was Ph.D. supervisor of S. Roy, Prof. T. Banerjee declared that S. Roy contributed just to the experimental part of the paper. Dr. J. Girovsky author of p3 and Prof. Taheri author of p6 did no reply to me.

Paper submitted on regular journals and/or present on arXiv:
a) T. C. van Thiel, J. Fowlie, **C. Autieri**, N. Manca, M. Šiškins, D. Afanasiev, S. Gariglio, and A. D. Caviglia, Bandwidth control of correlated spin-orbit semimetal $SrIrO_3$ through octahedral connectivity across oxide interfaces. Accepted to ACS Materials Letters (2019).
b) M. Asa, **C. Autieri**, R. Pazzocco, C. Rinaldi, W. Brzezicki, A. Stroppa, M. Cuoco, S. Picozzi, M. Cantoni, Anomalous Hall effect in antiferromagnetic/non-magnetic interfaces. Submitted to Phys. Rev. Lett. Preprint available at https://arxiv.org/abs/1904.03541
c) Wen Lei, Xing Ming, Shengli Zhang, Gang Tang, Xiaojun Zheng, Huan Li, Wei Wang and **C. Autieri**, Structural transition, metallization and superconductivity in quasi 2D layered PdS_2 under compression. Submitted to Phys. Rev. B. Preprint available at https://arxiv.org/abs/2002.09118
d) D. J. Groenendijk, **C. Autieri**, T. C. van Thiel, W. Brzezicki, P. Barone, N. Gauquelin, J. Verbeeck, A. Filippetti, S. Picozzi, M. Cuoco and A. D. Caviglia, Berry phase engineering at oxide interface. Submitted to Phys. Rev. Research. Preprint available at https://arxiv.org/abs/1810.05619
e) Xing Ming, **Carmine Autieri**, Huanfu Zhou, Jiafeng Ma, Xin Tang, Xiaojun Zheng, In-gap states with nearly free electron characteristics in layered structure trivalent iridates. Submitted to J. Phys.: Condens. Mat. Preprint available at https://arxiv.org/abs/1909.04562

GRANTS WON

a) 1 April-31 December 2012. Awarded with Della Riccia postdoctoral fellowship (http://theory.fi.infn.it/casalbuoni/dellariccia/). Budget: 12.000 euros.

b) 10 July 2017. Awarded with grant for the SEED project by the research Institute CNR-SPIN. The SEED proposal is funded with the aim of supporting one-year original and well-focused research projects by young researchers. Budget: 11.000 euros.

FELLOWSHIP

a) Supported by the Carl Tryggers Stiftelse (grant no. CTS 12:419) from 1 May 2013 to 30 April 2014.

b) Supported by the Carl Tryggers Stiftelse (grant no. CTS 13:413) from 1 May 2014 to 30 April 2015.

C. Autieri co-supervised the following master and Ph.D. students:

a) Giuseppe Cuono, Master thesis. Title: Electronic structure and magnetic properties of CrAs investigated using tight-binding method. Supervisor: Prof. C. Noce (Università degli studi di Salerno, Italy).

b) Esteban Puyuelo, Master thesis. Title: A study of atomic diffusion from first principle theory. Supervisor: Prof. Dr. B. Sanyal (Uppsala university, Sweden).

c) Giuseppe Cuono, Ph.D. thesis. Title: New features exhibited by transition metal pnictides. Supervisor: Prof. C. Noce (Università degli studi di Salerno, Italy).

C. Autieri is currently co-supervisor of the the following Ph.D. students:

d) Co-supervisor of the Ph.D student Rajibul Islam. Supervisor: Prof. Dr. hab. Tomasz Dietl (IFPAN Warsaw, Poland).

e) Co-supervisor of the Ph.D student Ghulam Hussain. Supervisor: Prof. Dr. hab. Tomasz Dietl (IFPAN Warsaw, Poland).

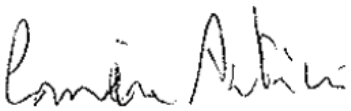

.....

(applicant's signature)